PCCP

ROYAL SOCIETY OF CHEMISTRY

PAPER

View Article Online
View Journal | View Issue

Cite this: *Phys. Chem. Chem. Phys.*, 2026, **28**, 120

Exploring the initial bond activations of PFAS on zero-valent iron

Glen R. Jenness, *[a] Elizabeth R. Zengel[bc] and Manoj K. Shukla*[a]

Ever since appearing in our society nearly 80 years ago, per- and polyfluoroalkyl substances (PFAS) have become a staple chemical used in a variety of consumer medical products. Unfortunately, these chemicals have been shown to be linked to a variety of health issues, including but not limited to, cancers, low birth rates, and suppressed immune systems. New guidance from the United States Environmental Protection Agency (USEPA) have given public water systems until 2029 to bring down the concentrations of perfluorooctanoic acid (PFOA) and perfluorooctanesulfonic acid (PFOS), two major PFAS molecules, to concentrations below 4.0 parts per trillion. In order to meet these goals it is imperative to develop chemical means of degrading PFAS molecules, which is hampered by the high strength C–F bond found in these compounds. Heterogeneous catalysis offers an attractive route for the degradation of these bonds, however progress along these lines have been hampered by a lack of knowledge regarding PFAS interactions and reaction energetics on a variety of catalyst materials. In a recent study (Jenness and Shukla, *Env. Sci. Adv.*, 2024, **3**, 383) we explored a set of 27 transition metals in order to assess their ability to cleave the C–F bond and found iron (Fe) to be a promising candidate as a PFAS degradation catalyst. Consequently, in this study we focus on the (110) surface of Fe and explore how perfluorobutanoic acid (PFBA, a common PFAS molecule and stand-in for PFOA) can react with the catalytic surface sites using density functional theory (DFT). Through the calculation of the thermodynamics and kinetics of 10 reactions, we are able to build a simple kinetic model that demonstrates that while Fe(110) has the ability to degrade the C–F bonds in PFBA the primary reaction route is through the degradation of the carboxylic acid head group.

Received 29th July 2025,
Accepted 26th November 2025

DOI: 10.1039/d5cp02901e

rsc.li/pccp

1 Introduction

Since their introduction in the 1940s,[1] per- and polyfluoroalkyl substances (PFAS) have found their way into a variety of consumer and medical goods.[1–4] Unfortunately, it has emerged in recent years that PFAS molecules are an environmental health threat.[3–7] PFAS contamination can occur through soil and groundwater sources[8–17] (which is further compounded by the presence of salt[18,19] and organic matter content[20,21]). Exposure through these environmental means results in PFAS accumulation in food chains,[22–24] oceans,[25] and prenatally in humans.[26] Cancers, low birth rates, and immune system issues have all been related to PFAS exposure.[27–29]

In May 2025 it was announced that the United States Environmental Protection Agency (EPA) will be keeping its current maximum contaminant levels (MCL) for the prominent PFAS molecules perfluorooctanoic acid (PFOA) and perfluorooctanesulfonic acid (PFOS).[6] This enforces the 2024 MCL guidance of 4.0 parts per trillion (ppt) for PFOA and PFOS, in addition to giving public water systems to 2029 to implement solutions to the PFAS problem if detected levels are above the cited MCLs.[7] However remediation is hampered by their use and ubiquitous nature in modern society, which is owed to the presence of multiple C–F bonds. These bonds are notoriously strong, with a bond dissociation energy of ~115–127 kcal mol^{-1}.[30–34] In order to contextualize this value, the carbon–hydrogen bond has a dissociation energy of 90–105 kcal mol^{-1},[31,33] the carbon–carbon bond 85–104 kcal mol^{-1},[31,35] and the carbon–oxygen bond 80–110 kcal mol^{-1}.[31] This is the reason PFAS molecules are referred to as "forever chemicals" in our common lexicon; the C–F bonds form a protective chemical sleeve that shields the more fragile bonds of the molecule and gives these molecules their unique physico-chemical properties.

There have been many reviews on the subject of PFAS remediation,[36–45] and remediation of PFAS saturated environs falls under two broad categories: capture and degradation. For the capture of PFAS, filtrants comprised of carbonaceous

[a] *Environmental Laboratory, US Army Engineer Research and Development Center, 3909 Halls Ferry Road, Vicksburg, Mississippi 39180, USA. E-mail: Glen.R.Jenness@usace.army.mil, Manoj.K.Shukla@usace.army.mil*
[b] *Department of Chemistry and Biochemistry, Old Dominion University, Norfolk, Virginia 23529, USA*
[c] *Oak Ridge Institute for Science and Education (ORISE), 1299 Bethel Valley Rd, Oak Ridge, Tennessee 37830, USA*

material[46–55] and polymers[56–58] are popular choices. Additional materials and techniques, such as nanomaterials,[59–62] thermal desorption,[63] stabilization and solidification (S/S),[64,65] mechanical manipulation,[66] adsorption onto clays[67–70] and fluorinated hydrogels[71,72] have been proposed. Our group in particular has previously published in this area, with prior studies looking at clays,[69] nanomaterials,[60,61] functionalized graphene,[52,53] and biomolecules.[48,73]

Alternatively, one can seek to destroy or chemically transform PFAS molecules. This not only allows us to prevent the re-release of toxic chemicals from a sorptive material,[74,75] but it also allows us to safely destroy existing stocks through their conversion to value-added chemicals. Degradation methods have included electrochemical methods,[32,76–84] sonochemically,[85–89] photochemical reduction,[90–92] thermal,[93] oxidation *via* activated persulfate,[89,94–96] plasma treatment,[97–99] microbial degradation,[100–102] chemically assisted degradations,[103–107] hydrothermal liquefaction,[75] low-temperature hydroxide-mediated decarboxylation and defluorination,[108,109] supercritical water oxidation,[110,111] metal catalysis,[30,112–122] ferrihydrate,[123] and treatment with zero-valent iron.[55,95,96,109,124–129]

It is this last degradation route that is of interest to the current study. Zero-valent iron (also known as Fe^0 or ZVI) is an iron-based catalyst in which non-oxidized iron donates electrons to the contaminant of interest. A long standing favorite in the remediation community, it has been a subject of numerous studies and reviews.[130–137] In a recent manuscript our group studied a set of 27 transition metals and examined their ability to donate electrons from the metal surface to the lowest-unoccupied molecular orbital (LUMO) of perfluorobutanoic acid (PFBA) through the Blyholder mechanism.[112] Detailed analysis of the electronic structure of the transition metal-PFBA complex revealed that bcc metals (like iron) transfer electrons more readily to the C–F bonds in PFBA than non-bcc metals. This facilitates the weakening of these bonds (as the LUMO has an anti-bonding character), and makes the cleavage of C–F bonds more energetically favorable. However, in that study we only considered the thermodynamics of the C–F bond, and as a consequence did not explore the kinetics or other reactions. Given the interest in utilizing iron (especially in its zero-valent form) in PFAS remediation, it is prudent to expand on this study by examining these factors and provide a detailed analysis on the early reaction steps of PFBA degradation.

This leads us to the focus of the current study. Here, we consider the low-index (110) surface of bcc-iron and its interaction with PFBA. The choice of PFBA is two-fold: firstly, in our prior work on metal surfaces we examined the molecular orbitals and electronic structure of PFBA and its larger cousin perfluorooctanoic acid (PFOA), and comparison of our results indicate that general trends in reactivity for PFBA can be transferred to PFOA. Secondly while a lot of the focus on PFAS involves PFOA, PFBA still is a PFAS of concern (in April 2025, the Illinois Environmental Protection Agency announced a health advisory limit of 0.0038 mg L^{-1}).[138] Additionally as PFBA is a four carbon chain (compared to PFOA's 8 carbons), it naturally lends itself to computational studies as it is large enough to catch the salient features whilst still be computationally tractable with *ab initio* methods.[112] In contrast to our prior work, we consider a set of 6 primary reactions and 4 secondary reactions (including, but not limited to, C–F scission from α- and β-carbons, decarboxylation, and deprotonation). In addition to the thermodynamics, we also calculated kinetic factors by consideration of the transition state energy and construction of a microkinetic model. Ultimately we find that while iron is capable of cleaving C–F bonds the majority of the first steps in PFBA degradation occurs through degradation of the head-group, which would result in oxidation of the iron surface. This indicates that the observed C–F scission products from experimental methods would ultimately come after and would appear later in the degradation process. Our results are, in part, supported by experimental results[96,109,125,128,129] and demonstrate why C–F scission products are observed the way they are. This paper is organized as follows: we begin with a discussion of our choice of reactions, then a discussion of our transition states and their associated energetics, followed by a discussion of the results of our microkinetic model and how we can relate our results to prior experimental studies. For those interested in the technical details a section on our computational methods is presented at the end of this paper in order to draw the attention more to our results rather than the techniques used.

2 Results and discussion

In the current study we consider six different elementary reactions for PFAS on a Fe(110) surface (in addition to a adsorption step); these reactions are shown in Table 1. **R0** is the adsorption of PFBA onto the Fe(110) surface; we use the two lowest energy conformers of PFBA on Fe(110) that we derived in our prior work (see Jenness and Shukla[112] for details). We begin by neglecting the presence of a solvent as our calculations will correspond more with bulk PFAS which is known to have a low dielectric constant due to the nonpolar nature of the fluorinated carbon chain (1.99–9.99) and as a consequence will have a negligible impact on reaction energetics and trends.[139] Moreover, we begin with PFBA in its neutral, protonated state as transition metals have been shown to adsorb carboxylic acids and alcohols in the protonated state with a subsequent deprotonationation step under ambient conditions (see Fig. 1).[140–147] This leads us to **R1**, which is a deprotonation reaction. **R2** and **R3** are fluorine removal reactions, either from the α- or β-carbon (respectively). For the carbo binding mode (as shown in Fig. 2a), we did not consider **R3** as this process would occur over a rather large distance from the Fe(110) surface, and consequently would resemble more of a gas-phase fluorine removal reaction. **R4** is the removal of the –COOH group, whilst **R5** and **R6** is its decomposition *via* either removal of the carbonyl oxygen (=O) or or the hydroxyl (–OH). Gao *et al.*[77] observed little-to-no C–C bond breaking products, which is supported by our prior observation[112] that the carbon backbone atoms have a low Fukui index indicating a low probability of

Table 1 Reactions considered in the current study

Label	Reaction[a]	Description
R0[b]	$CF_3C_\beta F_2C_\alpha F_2COOH + Fe(110) \underset{k_{des}}{\overset{k_{ads}}{\rightleftharpoons}} (CF_3C_\beta F_2C_\alpha F_2COOH)^*$	Binding of PFBA to the Fe(110) surface
R1	$CF_3C_\beta F_2C_\alpha F_2COOH \underset{k_{-1}}{\overset{k_1}{\rightleftharpoons}} CF_3C_\beta F_2C_\alpha F_2COO^- + H^+$	Deprotonation of PFBA
R2	$CF_3C_\beta F_2C_\alpha F_2COOH \underset{k_{-2}}{\overset{k_2}{\rightleftharpoons}} CF_3C_\beta F_2C_\alpha FCOOH^+ + F^-$	Removal of a –F from the C_α position
R3	$CF_3C_\beta F_2C_\alpha F_2COOH \underset{k_{-3}}{\overset{k_3}{\rightleftharpoons}} CF_3C_\beta FC_\alpha F_2COOH^+ + F^-$	Removal of a –F from the C_β position
R4[c]	$CF_3C_\beta F_2C_\alpha F_2COOH \underset{k_{-4}}{\overset{k_4}{\rightleftharpoons}} CF_3C_\beta F_2C_\alpha F_2^{\pm} + COOH^{\mp}$	Removal of the –COOH group from the C_α position
R5	$CF_3C_\beta F_2C_\alpha F_2COOH \underset{k_{-5}}{\overset{k_5}{\rightleftharpoons}} CF_3C_\beta FC_\alpha F_2COH^{2+} + O^{2-}$	Removal of a oxygen from the carboxylic acid group
R6	$CF_3C_\beta F_2C_\alpha F_2COOH \underset{k_{-6}}{\overset{k_6}{\rightleftharpoons}} CF_3C_\beta F_2C_\alpha F_2CO^+ + OH^-$	Removal of a hydroxyl (OH) from the carboxylic acid group
R7[d]	$CF_3C_\beta F_2C_\alpha F_2COOH \underset{k_{-7}}{\overset{k_7}{\rightleftharpoons}} CF_3C_\beta F_2C_\alpha FCOO + F^-$	Removal of a –F from C_α following deprotonation
R8	$CF_3C_\beta F_2C_\alpha F_2COOH \underset{k_{-8}}{\overset{k_8}{\rightleftharpoons}} CF_3C_\beta FC_\alpha F_2COOH + F^-$	Removal of a –F from C_β following deprotonation
R9	$CF_3C_\beta F_2C_\alpha F_2COOH \underset{k_{-9}}{\overset{k_9}{\rightleftharpoons}} CF_3C_\beta FC_\alpha F_2^- + CO_2$	Removal of a CO_2 following deprotonation
R10	$CF_3C_\beta F_2C_\alpha F_2COOH \underset{k_{-10}}{\overset{k_{10}}{\rightleftharpoons}} CF_3C_\beta F_2C_\alpha F_2CO^+ + O^{2-}$	Removal of an oxygen following deprotonation

[a] In **R1**–**R10** we use a notation that implies the assignment of a formal molecular charge to either the product(s) or reactant(s). We would like to note that usage of such a notation is due to pedagogical reasons and is designed to aid the reader in thinking about how the molecular fragments break apart. We also need to emphasis that the total charge in our calculations is zero (see Section 4.1 for the full computational details). [b] For **R0**, an asterisk (*) denotes a surface bound species. [c] The "charge assignment" for the product species is ambiguous; however the two products would have the opposite charge from them in order to maintain overall charge neutrality. [d] While we show the reactants to be a single PFBA anion as the result of the deproationation in **R1**, there is a counter proton on the Fe(110) surface in order to maintain charge neutrality. See Section 4.1 for more details.

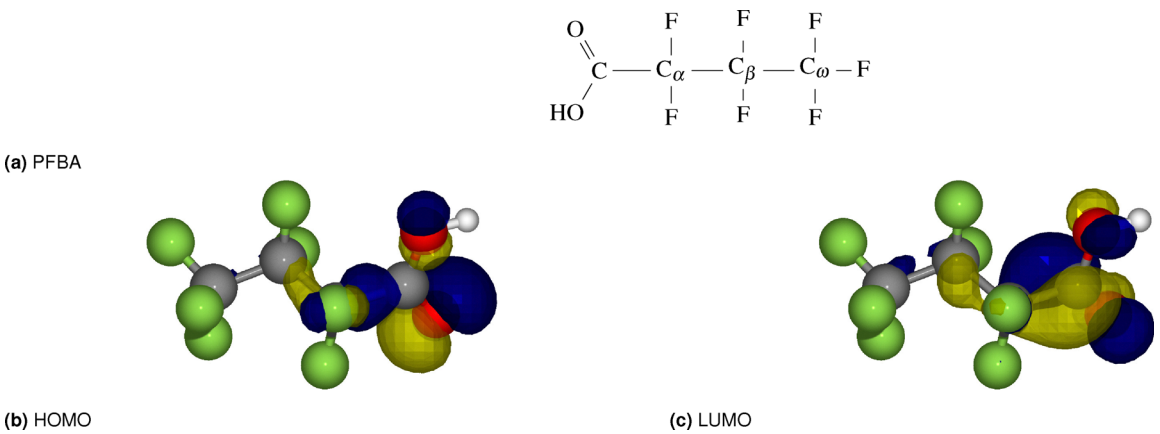

Fig. 1 Perfluorobutanoic acid (PFBA) and its highest occupied molecular orbital (HOMO) and lowest unoccupied molecular orbital (LUMO). (a) shows the carbon labeling scheme used in the current study, where in (b) and (c) we show the highest occupied molecular orbital (HOMO) and lowest unoccupied molecular orbital (LUMO) of PFBA.

reactivity. Consequently we do not consider any C–C bond breaking reactions outside of **R4** and **R9**, which has been observed by Gao *et al.*[77] **R7**–**R10** represent **R2**–**R5** following deprotonation of the PFBA. Even though not present in the equations of Table 1, **R7**–**R10** featured the presence of a surface bound hydrogen in order to ensure charge neutrality on the unit cell. We kept the surface bound hydrogen in the same position that was found for the final state of **R1** as we wish to capture the effect of the reverse reaction in our kinetic model shown below (see Section 4.2).

2.1 Primary reactions

In Table 2 we present the activation (E_a) and reaction (E_{rxn}) energies for the reactions in Table 1 for the binding modes in Fig. 2. We start our discussion with **R0**, which is the initial adsorbtion of PFAS onto the Fe(110) surface. Note that in

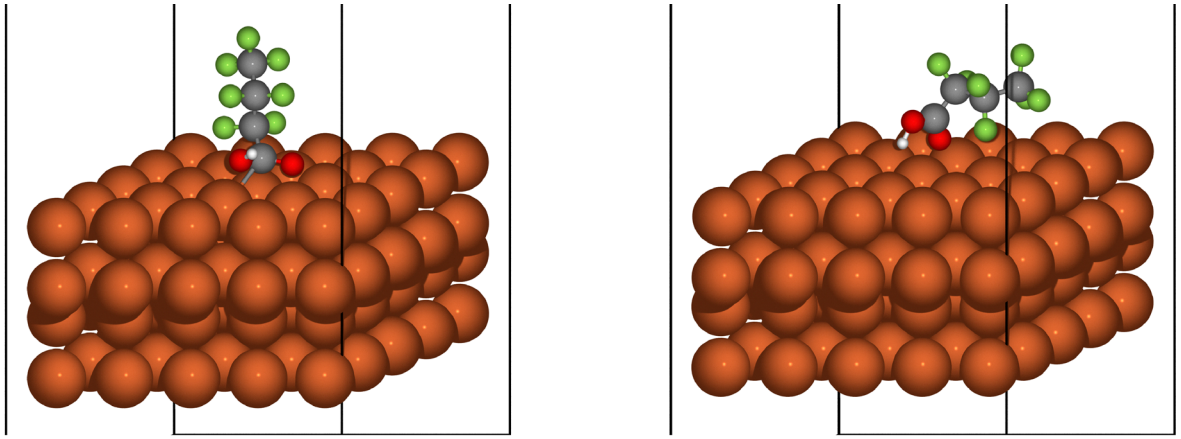

(a) "Carbo" binding mode (b) "Flat" binding mode

Fig. 2 The two binding modes of PFBA on Fe(110) using the geometries from Jenness and Shukla[112] optimized with the PBE functional. Solid black vertical lines denote the periodic boundary conditions in the *xy*-plane. Orange spheres are iron, grey carbon, red oxygen, white hydrogen, and green fluorine. In (a) the carbo binding mode is shown whilst in (b) the flat binding mode is shown.

Table 2 Reaction energetics for the binding modes of PFBA on Fe(110) as shown in Fig. 2. Units are in electron volts (eV)

	Carbo mode		Flat mode	
Reaction	E_a	E_{rxn}	E_a	E_{rxn}
R0		−1.43		−1.36
R1	0.47	−0.85	0.07	−1.40
R2	0.90	−0.99	0.60	−1.18
R3	Not applicable		0.70	−0.88
R4	0.86	−0.42	2.80	+1.87
R5	0.86	−0.26	0.37	−0.60
R6	0.25	−1.41	1.18	−0.78
R7	0.78	−0.92	1.05	−0.44
R8	Not applicable		1.03	−0.87
R9	1.73	+0.13	2.04	+1.15
R10	0.89	−0.65	0.81	−0.31

adsorption reactions the binding energy is equivalent with the reaction energy. From Table 2, we can see that the carbo mode has a binding energy of −1.43 eV whilst the flat binding mode has a binding energy of −1.36 eV; a difference of 0.07 eV. In order to ascertain how such a small difference in binding energies can influence the initial surface concentrations, we turn to the thermodynamic binding states model of Jenness and co-workers.[148–150] This technique modifies the Gibbs free energy of adsorption (G_{ads}) in the following fashion,

$$\Delta G_{ads} = G^{\circ}_{ads}(T) + k_B T \ln\left(\frac{C}{H \times P^{\circ}}\right), \quad (1)$$

where $G^{\circ}_{ads}(T)$ is the Gibbs free energy of adsorption referenced to atmospheric pressure, C is the concentration, H is the Henry's law constant of PFBA (we use the value of 1.24 Pa m^3 mol^{-1} from Kwan[151]), and P° is the reference pressure (1 atmosphere). For the concentration in eqn (1) we take it to be equal to one-half of the solubility limit (we use the solubility limit from Kwan[151]) of (3.15 mol m^{-3}). For the temperature we assume room temperature (25 °C).

Inclusion of the concentration term in eqn (1) shifts the binding energy for the flat binding mode from −1.36 eV to −1.29 eV. However for the carbo mode inclusion of the thermal corrections plus the concentration adjustment is nearly equal to the difference between the 0 K electronic energy of the PFBA-Fe(110) system and its thermal correction. This results in the terms canceling and as a result the binding energy is unchanged from the −1.43 eV value. Thus by including thermal and concentration corrections, the difference in the binding energies between the two binding modes increases to 0.14 eV, which is double of what we saw sans thermodynamics. If we insert the Gibbs free energy of binding into a Boltzmann distribution,

$$\text{Probability} = \frac{e^{-\Delta G_{ads,i}/k_B T}}{\sum_{i}^{\text{modes}} e^{-\Delta G_{ads,i}/k_B T}} \times 100, \quad (2)$$

we can determine the probability of which binding mode is dominant. In doing so, we find the carbo binding mode has a probability of being favored of 99.6%, whereas the flat binding is only 0.4%. However we would like to emphasize that this result is mainly to demonstrate how such a small change in the binding energy can result in a drastic change in the concentration of either binding mode, and in order to ascertain which mode is more preferred from a thermodynamic perspective one would need to include more binding states featuring things like the presence of solvent (either implicit or explicit). Thus we will treat the initial concentrations the same for both modes when we construct our kinetic model (eqn (5)).

Moving on to the deprotonation reaction in **R1**, the O–H bond length (r_{O-H}) starts with a value of 0.98 Å and 1.03 Å for the carbo and flat modes, respectively. In both binding modes the ∠COH becomes more obtuse which results in the H atom being oriented towards the Fe(110) surface at a bcc-hollow site. Comparison with the gas-phase value of 0.98 Å reveals that the flat mode has a slightly more "activated" O–H bond as denoted

by its slightly increased bond length. Moving along the reaction coordinate, we find that the r_{O-H} at the transition state elongates to 1.28 Å and 1.19 Å for the carbo and flat modes, respectively, with the hydrogen atom coming to rest in a bcc-hollow site in the final state (see Fig. 3). In terms of energetics, we find that the carbo mode has a significantly weaker reaction energy and higher activation barrier than the flat mode. While this might seem counter-intuitive at first (recall the carbo mode has a greater degree of contact with the head group to the Fe(110) surface, and therefore we would expect a lower barrier and a more exothermic reaction energy), we attribute the difference to geometrical effects. Consideration of the reaction pathways shown in Fig. 3 shows that as the flat mode undergoes deprotonation the resulting –COO* head group forms a closer assocation to the Fe(110) surface, which results in an increased stabilization of the deprotonated PFBA. Consequently it is this enhanced stability that results in a lower activation barrier and reaction energy. In Tables S2 and S10 we show the Bader charges[152–155] for the initial, transition, and final states of **R1**. For clarity, we only show the Bader charges of the PFBA and related atoms as the opposite (but equal) charge is distributed all throughout the Fe(110) surface. The majority of the atomic charges are consistent across all three states, with the exception of the acid C and the hydrogen; here we see that the acid C accumulates a positive charge whereas the hydrogen goes from positive to negative.

In **R2** and **R3** we have a C–F bond breaking at the alpha and beta carbon positions, respectively. For **R2**, the fluorine is bound to a Fe–Fe bridge on the Fe(110) surface. The C_α–F bond in the gas-phase has a length of 1.36 Å; in the flat binding mode this increases slightly to a bond length of 1.38 Å and for the carbo binding mode it is relatively unchanged from the gas-phase value. In the transition state the C_α–F bond elongates to a value of 1.88 Å and 1.66 Å for the carbo and flat modes, respectively. The initial, transition, and final states for both modes are shown in Fig. 4. From Table 2 the reaction energies (E_{rxn}) are −0.99 eV and −1.18 eV for carbo and flat binding modes, respectively. These values are lower in magnitude from our prior study[112] of −1.64 eV and −1.96 eV. This is due our current study using the PBE functional as opposed to the optPBE-vdW functional of our prior work, as discussed in Section 4.1. In terms of kinetics, the activation barriers (E_a) are 0.90 eV and 0.60 eV for carbo and for flat binding mode, respectively. This is a rather curious result as the carbo mode has a C_α–F bond that is closer to the surface than the flat mode and as a consequence, we would expect that mode to be more energetically favored. It is plausible that the geometry of the transition state complex for the flat mode provides a stabalizing effect, which would lower the barrier.

For **R3** (see Fig. 5), we could not locate a reaction in which only a F_β is removed for the carbo mode; in all attempts C_β–F scission was accompanied with a simultaneous C_α–F scission reaction. As such we only considered C_β–F scission for the flat binding mode. Similar to the C_α–F bond, the C_β–F bond has a length of 1.36 Å in the gas-phase. Upon adsorption to the Fe(110) surface, this lengthens a negligible amount to 1.37 Å. In the transition state the C_β–F bond becomes 1.49 Å, indicating an early transition state. Energetically, this reaction has a E_{rxn} of −0.88 eV and an E_a of 0.70 eV.

In Table S3 we report the Bader charges for **R2** in the carbo mode; here we can readily see that as the reaction proceeds the C_α

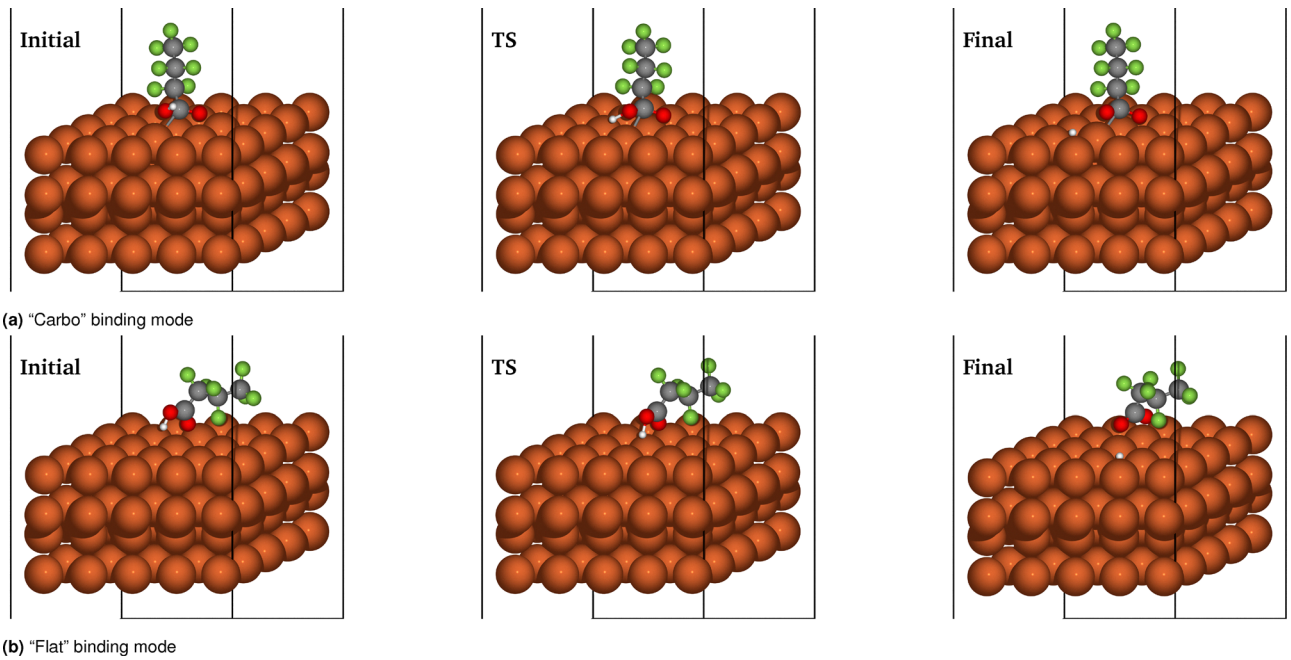

Fig. 3 Initial, transition (TS), and final states for **R1** for the two binding modes. Solid black vertical lines denote the periodic boundary conditions in the *xy*-plane. Orange spheres are iron, grey carbon, red oxygen, white hydrogen, and green fluorine. In (a) the initial, transition (TS), and final state for the carbo mode is shown, whilst in (b) the same for the flat mode is shown.

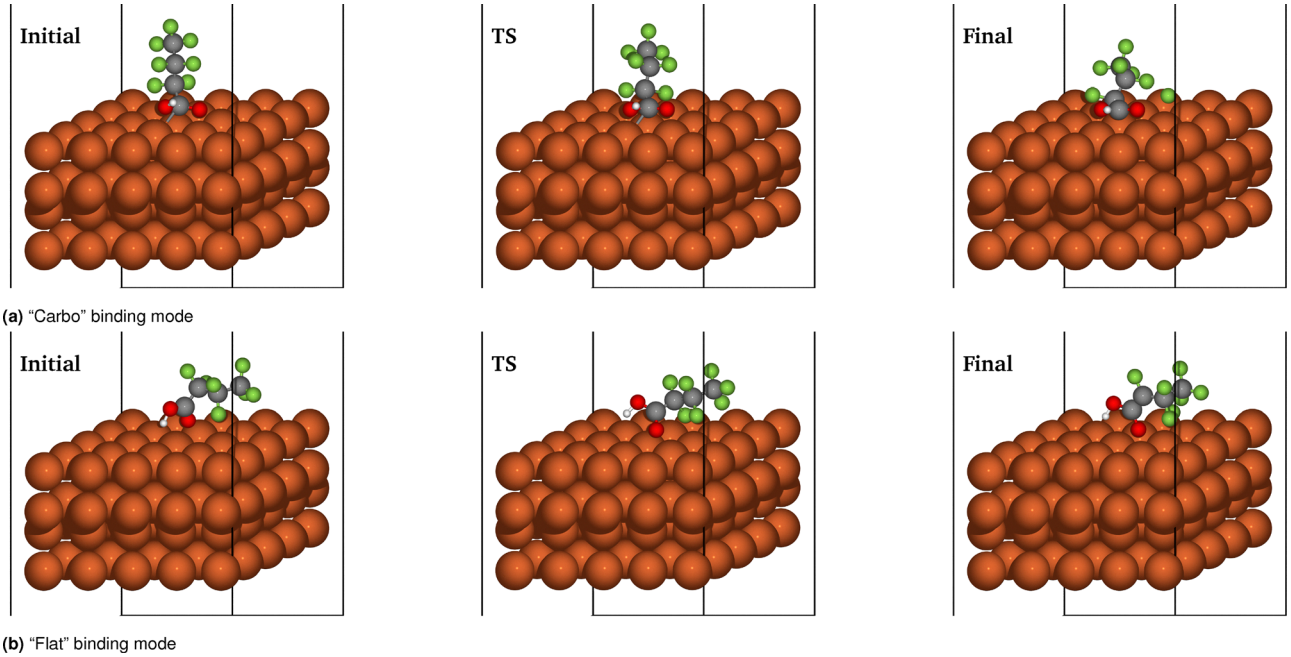

Fig. 4 Initial, transition (TS), and final states for **R2** for the two binding modes. Solid black vertical lines denote the periodic boundary conditions in the *xy*-plane. Orange spheres are iron, grey carbon, red oxygen, white hydrogen, and green fluorine. In (a) the initial, transition (TS), and final state for the carbo mode is shown, whilst in (b) the same for the flat mode is shown.

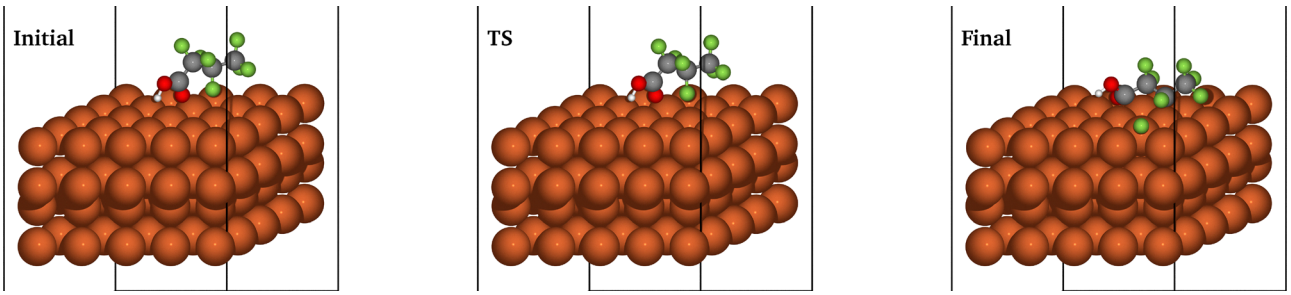

Fig. 5 Initial, transition (TS), and final states for **R3** for the flat binding mode. Solid black vertical lines denote the periodic boundary conditions in the *xy*-plane. Orange spheres are iron, grey carbon, red oxygen, white hydrogen, and green fluorine.

atom gains a negative charge (with the F_α) atom gaining a negligible charge ($\Delta Q < 0.1$). A similar trend is observed for **R2** and **R3** for the flat mode; from Tables S11 and S12 the C_α and C_β atoms both aquire a negative charge indicating a donation of electron density from the Fe(110) surface to the C–F bonds. This supports our earlier assertion that the chemistry of PFAS degradation occurs through a Blyholder back-bonding mechanism.[112]

R4 is the first of three reactions that concerns the carboxylic head group (–COOH). In this reaction, the C–C bond between the C_α and the carbon in the acid head group undergoes scission. In both binding modes, the $CF_3CF_2CF_2$ moiety is bound to a nearby Fe atom; however the fate of the –COOH is different between the two modes. For the carbo mode, the –COOH has the carbon atom bound to the surface through a bridge site with the carbonyl oxygen laying in a bcc-hollow site with the C═O bond being parallel to the Fe(110) surface (see Fig. 6a). The final state for the flat mode has the oxygens pointed towards the surface, with the carbonyl oxygen centered above a bcc-hollow site (see Fig. 6b). Geometrically speaking, the gas-phase C_α–COOH bond has a length of 1.57 Å; upon adsorbtion this bond contracts slightly to 1.55 Å and 1.53 Å for the carbo and flat modes, respectively. In the carbo binding mode, this bond elongates to 2.01 Å in the transition state and has an exothermic E_{rxn} of −0.42 eV and an E_a of 0.86 eV. In contrast the flat binding mode has a C_α–COOH bond of 2.59 Å in the transition state and an endothermic E_{rxn} of 1.87 eV (with an E_a of 2.80 eV). This is a significant change from the carbo binding mode and comparison of these values with the other reaction energetics in Table 2 reveals that scission of the C_α–COOH for the flat binding mode is heavily disfavored and therefore unlikely to occur. It is plausible that the final state reported here is due to a *meta*-stable local minima; therefore we perturbed the final state geometry and reoptimize. However, this resulted in a minor change in the reaction energy of less

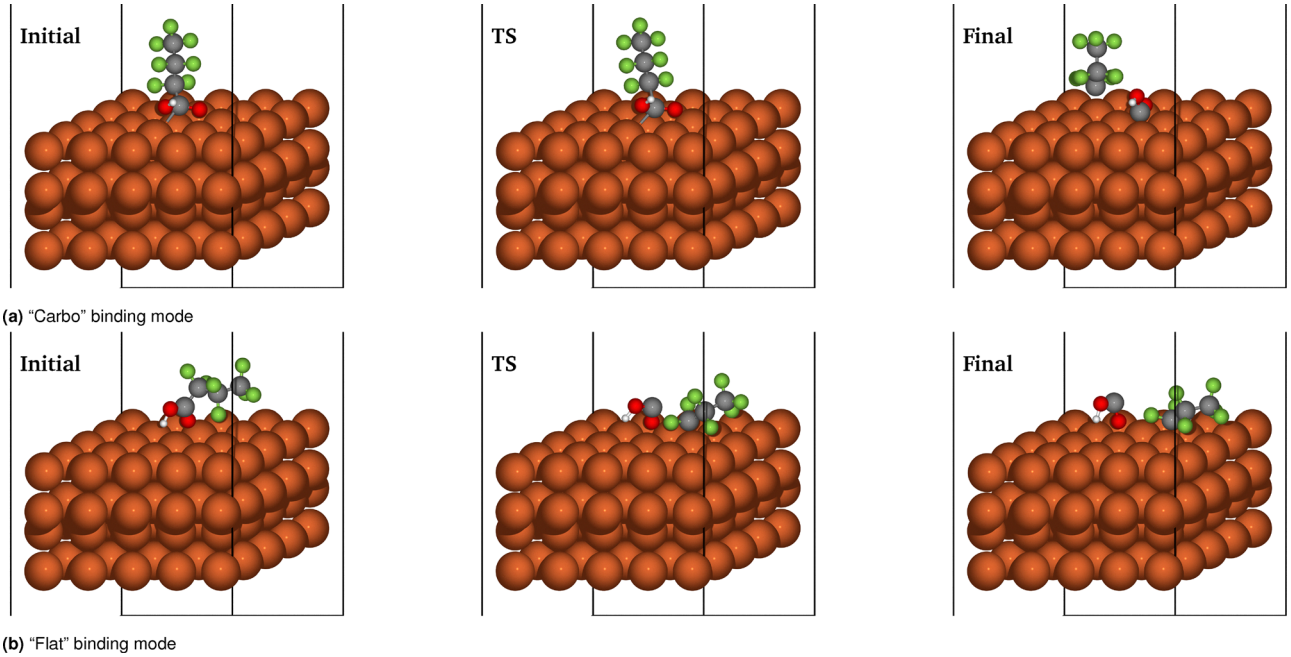

Fig. 6 Initial, transition (TS), and final states for **R4** for the two binding modes. Solid black vertical lines denote the periodic boundary conditions in the *xy*-plane. Orange spheres are iron, grey carbon, red oxygen, white hydrogen, and green fluorine. In (a) the initial, transition (TS), and final state for the carbo mode is shown, whilst in (b) the same for the flat mode is shown.

than 0.05 eV. Therefore we conclude that this reaction energy is due to a stable final state and is physically motivated.

In Tables S4 and S13 we report the Bader charges for the three reaction states for **R4**. As we break a C–C_α bond, we find that the Fe(110) surface donates electrons to this bond resulting in an accumulation of electron charge on both atoms as the reaction proceeds. For the carbo mode, we find that a small amount of charge is added to the C_α position in the transition state with the final state accumulating the most charge. Conversely, the acidic C has a negligible change in the charge ($\Delta Q < 0.1$). For the flat binding mode while the overall net charge transfered to the C_α position is the same as we observed in the carbo binding mode (~ 0.4), we find that the charge is primarily transferred to the transition state. This is rather curious given the anti bonding nature of the LUMO of PFBA (see Fig. S2 from Jenness and Shukla[112]) as we would expect adding electron charge would occupy this LUMO leading to a greater anti bonding character of this bond. However, as the degree of charge transfer between the surface and an adsorbate is orientation dependent[156,157] we conclude that the increase in E_{rxn} and E_a is due to a disfavorable orientation of the PFBA LUMO in the region of the C–C_α bond and the Fe(110) surface.

In the second head group reaction we consider the scission of the C═O bond in **R5**. In the gas-phase this bond has a length of 1.20 Å which lengthens to 1.37 Å in the carbo binding mode and 1.25 Å in the flat bonding mode. The fact that the C═O bond is longer in the carbo mode than the flat is due to the stronger surface interactions between the carboxylic acid head group and the Fe(110) surface. Following dissociation the carbonyl oxygen is found in a bcc-hollow site, as shown in Fig. 7. As the reaction proceeds, the C═O bond length increases to 2.00 Å for the carbo mode and 1.98 Å for the flat binding mode. This gives us barriers of 0.86 eV and 0.37 eV, and reaction energies of −0.26 eV and −0.60 eV for the carbo and flat modes, respectively. From Fig. 7b we can see that as the carbonyl oxygen is removed from the acid head group the number of interactions between the Fe(110) surface and PFBA increases and therefore results in a more stable complex.

Comparison of the Bader atomic charges explain this trend. From Tables S5 and S14 we can see that the carbon atom of the carbonyl acid group gains whilst the oxygen atom loses electrons. Interestingly, it is the flat bind mode that has the largest change in charge with the carbon atom gains $\sim 2\times$ as much electrons as we saw for the carbo mode. Therefore we attribute the increased exothermicity and lower barrier of the flat mode to the enhanced stability of this complex, which results in a greater degree of electron charge being donated from the surface to the PFAS.

The last reaction we considered as part of the primary reaction series is the dehydroxylation of the carboxylic acid group. Gas-phase PFBA has a C–OH bond length of 1.35 Å; this bond lengthens to 1.46 Å in the carbo binding mode and contracts slightly to 1.31 Å in the flat binding mode. At the transition state, these bonds elongate to 1.83 Å and 1.75 Å, respectively. In the final state the abstracted –OH species lies in a bcc-hollow binding site. From Table 2 we can see that the carbo binding mode has a reaction energy of −1.41 eV with a barrier of 0.25 eV; conversely, the flat mode has a reaction energy of −0.78 eV and a barrier of 1.18 eV. Given the oxyophillic nature of iron and the σ-bond nature of the C–OH bond,

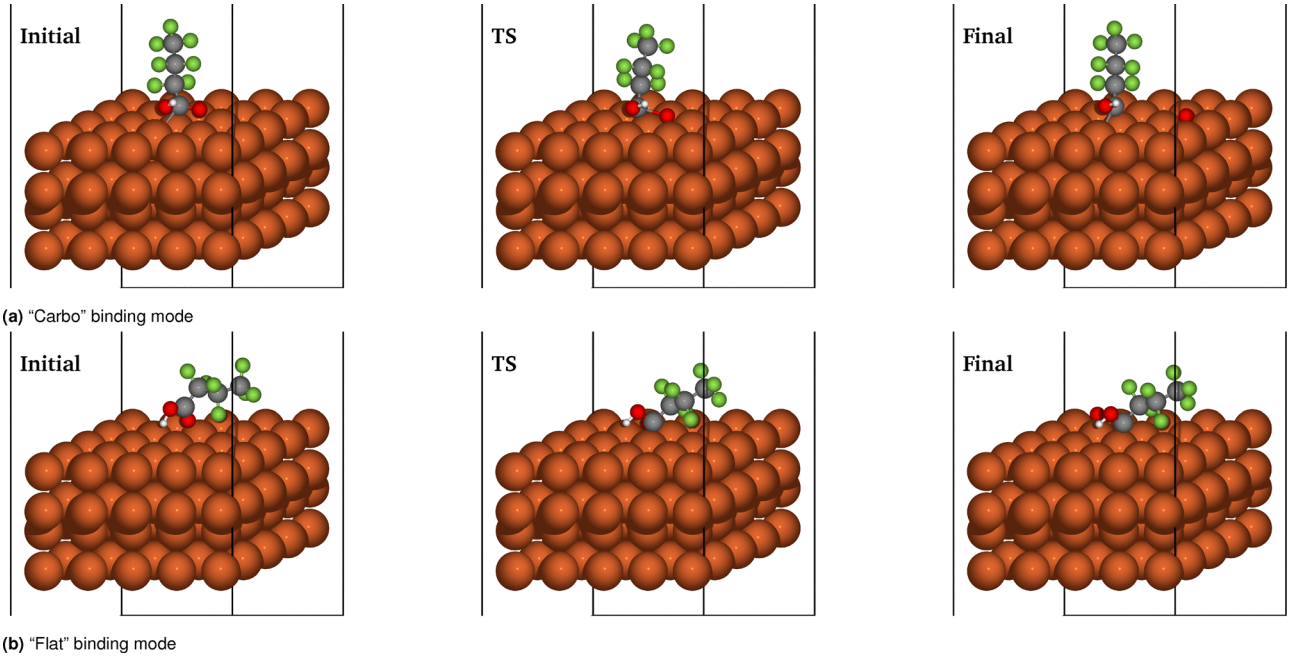

Fig. 7 Initial, transition (TS), and final states for **R5** for the two binding modes. Solid black vertical lines denote the periodic boundary conditions in the *xy*-plane. Orange spheres are iron, grey carbon, red oxygen, white hydrogen, and green fluorine. In (a) the initial, transition (TS), and final state for the carbo mode is shown, whilst in (b) the same for the flat mode is shown.

it is unsurprising the dehydroxylation of PFBA is exothermic. Moreover, the lower barrier and more exothermic reaction energy for the carbo mode can be explained in terms of geometry (see Fig. 8); as the carbo mode is closer to the surface, it is more acceptable to be activated by the Fe(110) surface. Consequently, the C–OH bond ends up being longer (as seen in the $\sim$0.10 Å increase in the bond length for the adsorbed complex) and as a result carries a significantly lower barrier and reaction energy. Analysis of the Bader charges in Tables S5 and S14 also gives further support for the geometric factors governing the above trend. From Table S1 we find that the charge on the carboxylic acid carbon change from $1.6e^-$ to $0.8e^-$ for the carbo binding mode, and $1.5e^-$ for the flat binding mode. This loss of positive charge denotes that this carbon atom gained electron density, which according to the Blyholder process would weaken the associated bonds (in this case the C–OH bond). As the carbo mode has a greater degree of charge transfer, it would be logical to associate this change in charge with the enhanced exothermicity of this reaction. Finally we wish to point out that in the final state of the flat mode for **R6** as the hydroxyl separates from the PFBA following the transition state that the hydrogen is pulled off the –OH moiety and onto the carbon atom of the former caboxylic acid group (see Fig. 8b). In looking at the reaction pathway there is no barrier associated with this process.

2.2 Secondary reactions following deprotonation

It has been known for a few decades that iron surfaces can deprotonate alcohols and carboyxlic acids, leading to the formation of surface bound alkoxy and carboxy species[140–144] that can undergo further degradation or reaction. As disccussed above for **R1**, Fe(110) can deprotonate the carboxylic acid group of PFBA in an exothermic fashion with a very low activation barrier ($<$0.5 eV). Consequently, we explored **R2–R5** with a deprotonated PFBA in order to ascertain how deprotonation affects the degradation of PFAS. In order to maintain charge neutrality in the following calculations, the proton is located on the surface in a nearby bcc-hollow site.

R7 is the removal of a fluorine atom from the C_α position and is shown in Fig. 9 for both binding modes. In the gas-phase the C_α–F bond is 1.39 Å; upon deprotonation of the –COOH group of PFBA this bond contracts slightly to 1.37 Å and 1.36 Å for carbo and flat modes, respectively. In the transition state these bond lengths lenghten to [1.71 Å] and 1.77 Å, respectively. As disccussed earlier for **R2** molecular PFBA had transition state C_α–F bonds of 1.88 Å and 1.66 Å for carbo and flat, respectively. Unlike what we observed for molecular PFBA, the fluorine ends up in a bcc-hollow instead of a Fe-Fe bridge. Energetically, deprotonation of the PFBA molecule in the carbo binding mode leads to an E_a of 0.78 eV with an E_{rxn} of -0.92 eV; contrast these values with the molecular PFBA of E_a of 0.90 eV and an E_{rxn} of -0.99 eV. The deprotonated flat binding mode carries an E_a of 1.05 eV (compared to 0.60 eV) and an E_{rxn} of -0.44 eV (compared to -1.18 eV). Comparison of Tables S3–S7 for the carbo mode shows that the Bader charges on the C_α carbon of PFBA changes negligibly following deprotonation. Examination of the final state Bader charges also reveals deprotonation has a negligible effect on the thermodynamics (which is further validated by the less than 0.1 eV change in the E_{rxn} between **R2** and **R7**). In the transition state, we observe a $0.15e^-$ charge difference between **R2** and **R7**. A similar comparison of Tables S11 and S16 for the flat mode can also be made,

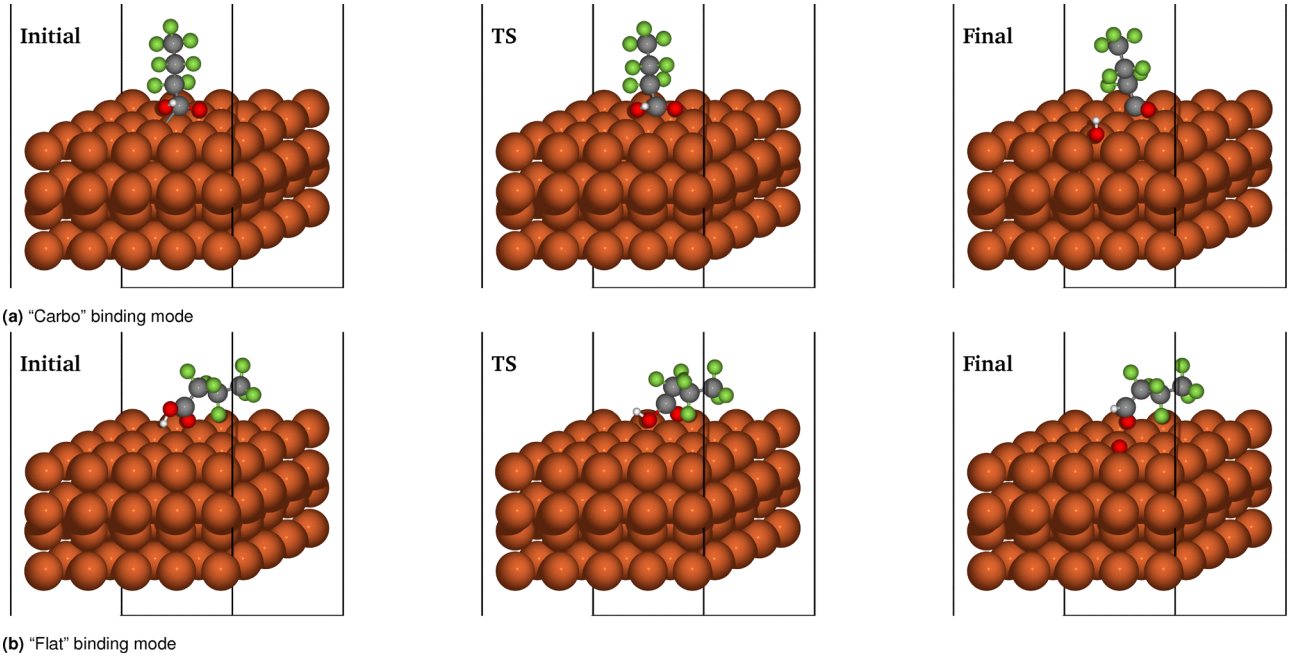

Fig. 8 Initial, transition (TS), and final states for **R6** for the two binding modes. Solid black vertical lines denote the periodic boundary conditions in the *xy*-plane. Orange spheres are iron, grey carbon, red oxygen, white hydrogen, and green fluorine. In (a) the initial, transition (TS), and final state for the carbo mode is shown, whilst in (b) the same for the flat mode is shown.

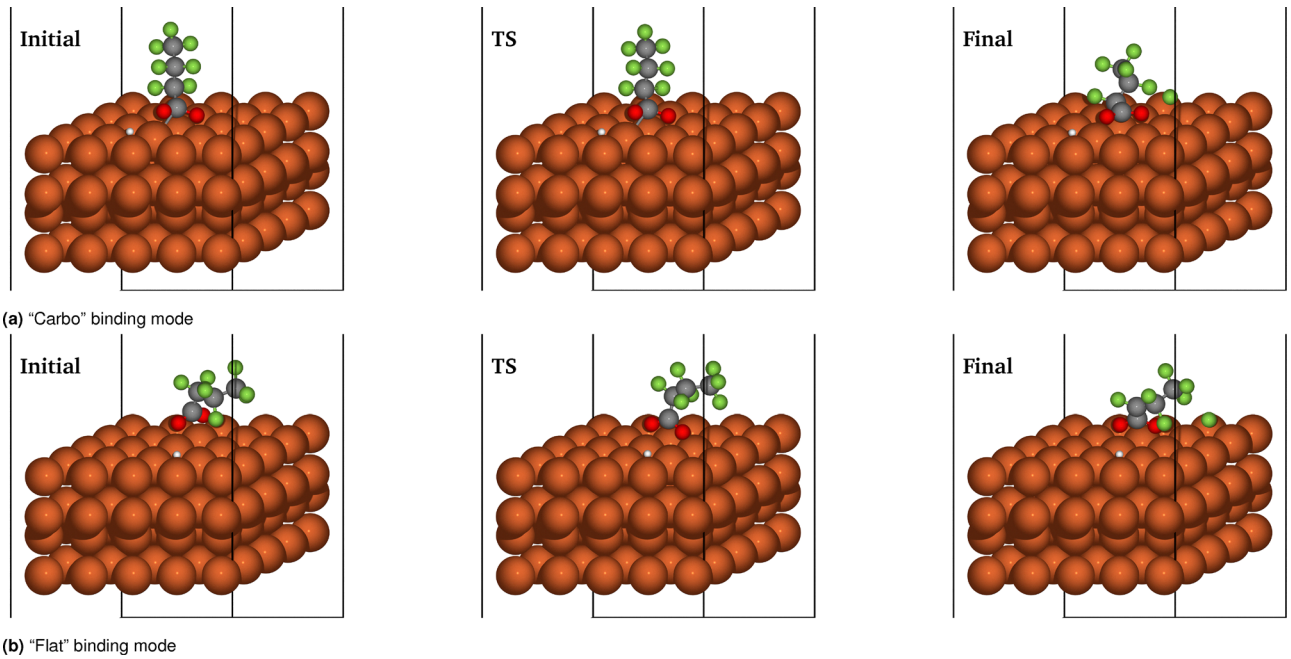

Fig. 9 Initial, transition (TS), and final states for **R7** for the two binding modes. Solid black vertical lines denote the periodic boundary conditions in the *xy*-plane. Orange spheres are iron, grey carbon, red oxygen, white hydrogen, and green fluorine. In (a) the initial, transition (TS), and final state for the carbo mode is shown, whilst in (b) the same for the flat mode is shown.

and reveal a similar trend to the carbo mode. Thus we conclude that the changes in the reaction energetics upon deprotonation of PFBA cannot be explained purely in terms of a Bader charge analysis.

Fig. 10 shows the initial, transition, and final states for **R8**, which deals with the removal of a fluorine from the C_β position of PFBA. Similar to what we observed for molecular PFBA the C_β–F bond in the deprotonated PFBA is unchanged from its gas-

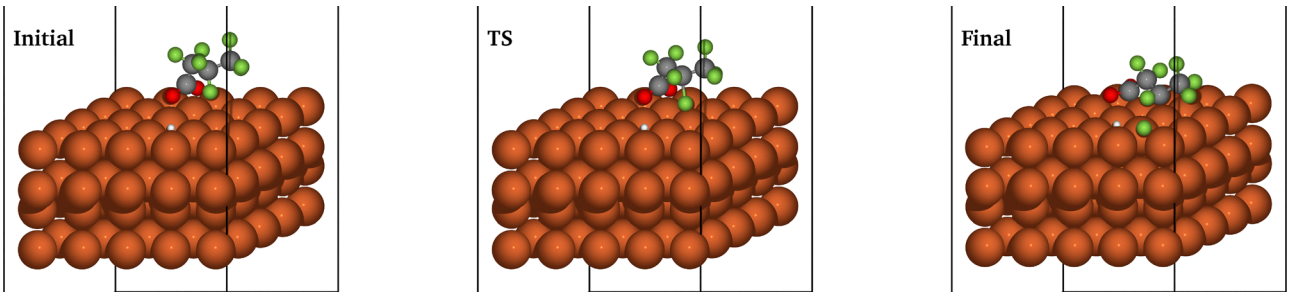

Fig. 10 Initial, transition (TS), and final states for **R8** for the flat binding mode. Solid black vertical lines denote the periodic boundary conditions in the *xy*-plane. Orange spheres are iron, grey carbon, red oxygen, white hydrogen, and green fluorine.

phase value (with a bond length of 1.38 Å for the adsorbed state, which is the same as the gas-phase value for this bond). In the transition state this bond lengthens to 1.82 Å, which is significantly longer than the transition state for molecular PFBA (1.49 Å). This increased bond length at the transition state leads to E_a changing from 0.70 eV for molecular PFBA to 1.03 eV for the deprotonated PFBA. Curiously enough however, the reaction energy remains relatively unchanged (−0.88 eV *vs.* −0.87 eV for molecular and deprotonated PFBA, respectively). Similar to what we observed for the carbo mode of **R3**, we could not locate a stable transition state for the removal of fluorine from the C_β position. Examination of the Bader charges in Tables S12 and S17 shows that the transition state for **R8** the C_β position accumulates more electron density than in **R3**, which provides an explanation for the changes in the reaction energetics discussed above.

R9 is the removal of a CO_2 from deprotonated PFBA. The C_α–COO bond is 1.61 Å in the gas-phase and upon adsorption and deprotonation of PFBA it assumes a bond length of 1.54 Å for both the carbo and flat modes; this is due to the similarity in the –COO binding motiff to the Fe(110) surface for the two modes (see Fig. 11). For the carbo mode the C_α–COO bond becomes 1.97 Å in the transition state and has an E_a of 1.73 eV and an E_{rxn} of +0.13 eV. While this reaction has a C–C_α bond that is shorter than what is observed for molecular PFBA, the reaction energetics are far less favorable when we consider deprotonated PFBA (recall molecular PFBA had an E_a of 0.86 eV and an E_{rxn} of −0.41, see Table 2). Examination of the flat mode shows a very similar result as molecular PFBA in the same binding mode; the transition state is 2.60 Å for deprotonated PFBA, with an E_a of 2.04 eV and an E_{rxn} of +1.87 eV. These results indicate that deprotonation of PFBA would result in a decrease of CO_2 formation. From Tables S4 and S8 for the carbo mode we can see that while the Bader charges for the C_α position are relatively unchanged for the final state, in the transition state **R9** results in a greater accumulation of electron

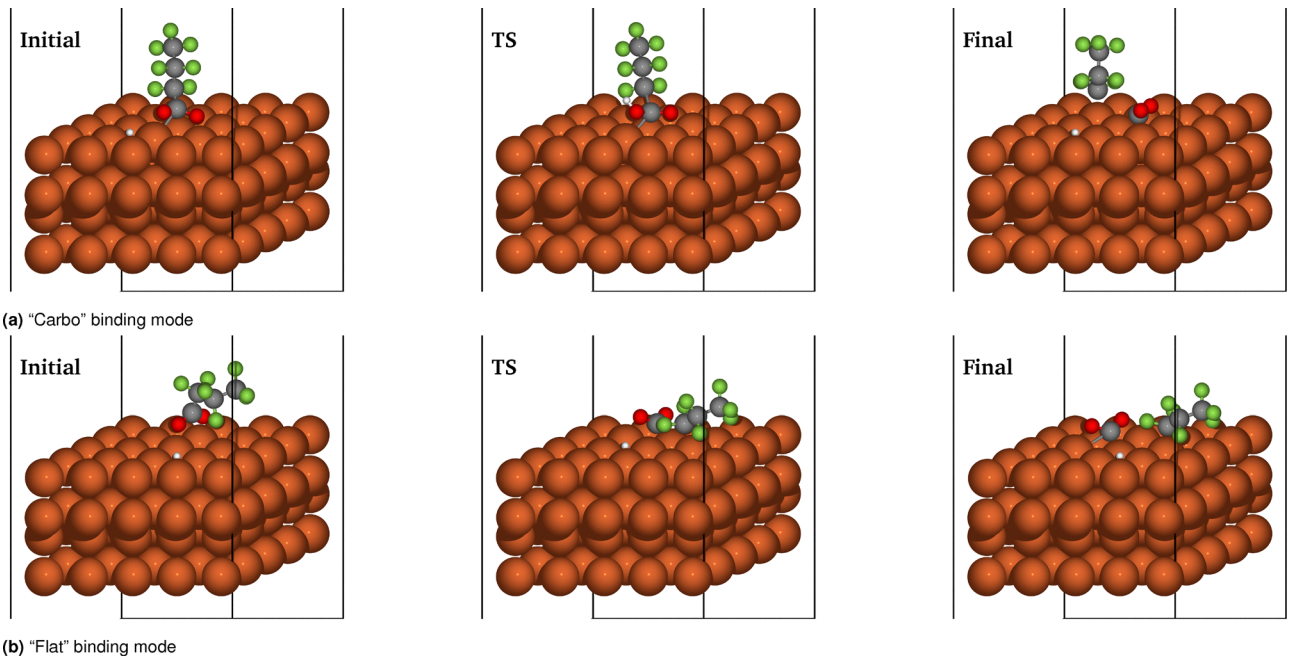

Fig. 11 Initial, transition (TS), and final states for **R9** for the two binding modes. Solid black vertical lines denote the periodic boundary conditions in the *xy*-plane. Orange spheres are iron, grey carbon, red oxygen, white hydrogen, and green fluorine. In (a) the initial, transition (TS), and final state for the carbo mode is shown, whilst in (b) the same for the flat mode is shown.

density than what we observed in **R4**. In addition, the acid carbon also accumulates more negative charge than what we saw in **R4**. For the flat mode, the Bader charges in Tables S13 and S18 show a similar trend for the C_α position as we observed for the carbo binding mode; however when we examine the charges for the acid carbon we find that deprotonation leads to a greater accumulation of electron charge in both the transition and final state.

Our final reaction considered is **R10** in which an oxygen atom is removed from the –COO head group (Fig. 12). In the gas-phase, the –COO group has a C–O bond length of 1.25 (which is slightly longer than the carbonyl bond length of 1.20 Å for molecular PFBA). In the gas-phase we expect the two C–O bonds to be equivalent; however on the surface one C–O bond lengthens to 1.37 Å and the second C–O bond lengthens to 1.31 Å upon adsorbtion for the carbo binding mode. The Bader charges in Table S9 show that in the initial state both oxygens have a similar charge, indicating that both oxygens are approximately equivalent. In choosing which C–O bond to break for this reaction, we opted for the one that was longer (*i.e.*, the C–O bond furthest from the surface hydrogen). At the transition state the C–O bond becomes 1.72 Å and has an E_a of 0.98 eV with an E_{rxn} of −0.65 eV; this is certainly more kinetically favorable than the C═O scission in **R5**, but is not as energetically favorable as the C–OH scission of **R6**. Turning back to Table S9 we can see that the Bader charges for the acid carbon gain a slight electron charge at the transition state with the final state accumulating the majority. Similar to **R5** (see Table S5) the oxygen atom being moved gains a slight positive charge, indicating a loss of electron density.

In contrast the flat binding mode as an adsorbed C–O bond length of 1.27 Å for both, which is not appreciably different from the gas-phase value. As both bonds are equivalent, we chose to split the C–O bond that is furtherest from the surface hydrogen in order to remain consistent with the carbo mode. Similar to the carbo binding mode the C–O transtion state bond length is 1.75 Å with an E_a of 0.81 eV and an E_{rxn} of −0.31 eV. While **R5** is more energetically favored, **R10** for the flat mode is more kinetically favored than **R6** (albeit it is not as thermodynamically favored). Regardless, both binding modes have a similar final state wherein the oxygen is located at a bcc-hollow and the $CF_3CF_2CF_2CO$ fragment is bound to an iron top site. From Table S19 we can see that the amount of electron density transfered to the PFBA in the flat mode is greater than what we observed for the carbo mode (Table S9). This provides a partial explanation as to why there is a decrease in the E_a for the two modes.

2.3 Kinetic model

Using the activation barriers and energies in Table 2 we ran the kinetic model discussed in Section 4.2 at temperatures of 25 °C and 100 °C with run times of a nanosecond (ns), a microsecond (μs) and a full second (s). We set the molecular concentration of PFBA to be equal to unity in order to better determine relative concentrations and percentages and the results are shown in Tables 3 and 4.

Starting with a temperature of 25 °C and the carbo binding mode the PFBA concentration decreases to 93.70% after 1 ns of runtime (see Table 3); the major products observed are $CF_3CF_2CF_2CO/OH$ with a trace of $CF_3CF_2CF_2COO/H$. This

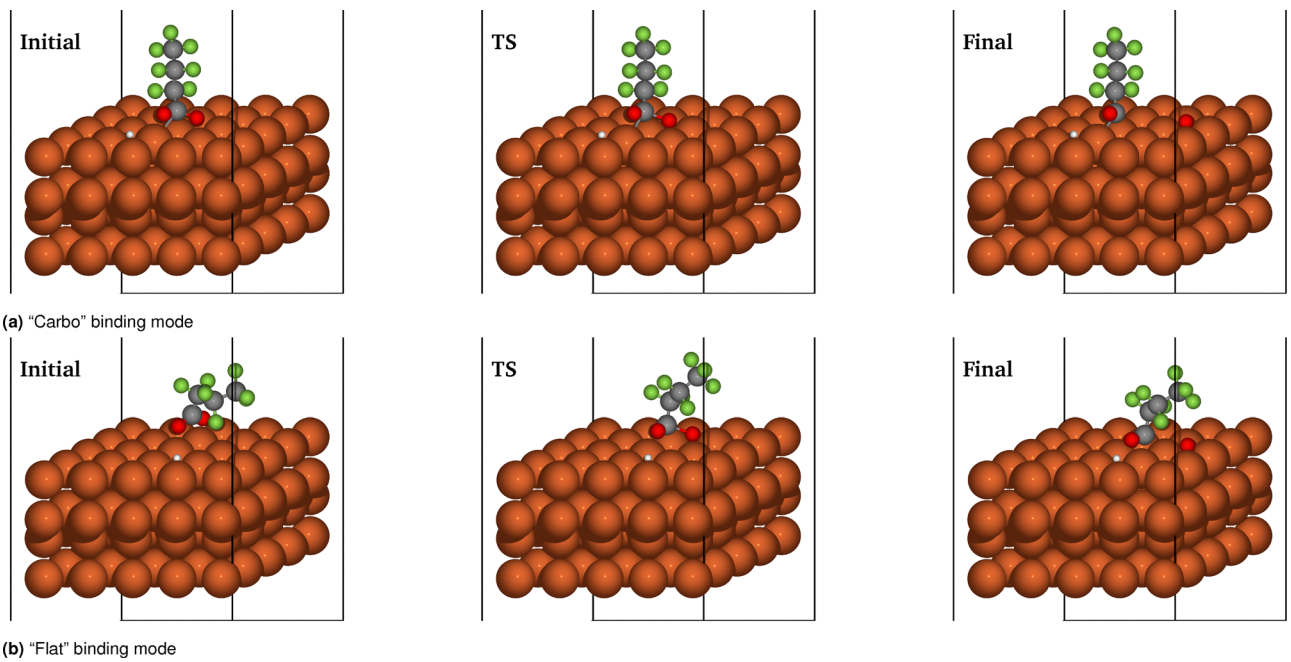

Fig. 12 Initial, transition (TS), and final states for **R10** for the two binding modes. Solid black vertical lines denote the periodic boundary conditions in the *xy*-plane. Orange spheres are iron, grey carbon, red oxygen, white hydrogen, and green fluorine. In (a) the initial, transition (TS), and final state for the carbo mode is shown, whilst in (b) the same for the flat mode is shown.

Table 3 Percent concentrations of the species in Table 5 resulting from the kinetic model in eqn (5) as a function of time scale for the carbo binding mode

	Time scale		
Species[a]	1 ns	1 μs	1 s
T = 25 °C			
PFBA	93.70	0.00	0.00
$CF_3CF_2CF_2CO$	6.27	100.00	100.00
$CF_3CF_2CF_2COO$	0.03	0.00	0.00
OH	6.27	99.49	99.49
O	0.00	0.51	0.51
H	0.03	0.51	0.51
T = 100 °C			
PFBA	57.64	0.00	0.00
$CF_3CF_2CF_2CO$	42.00	100.00	100.00
$CF_3CF_2CF_2COO$	0.36	0.00	0.00
OH	41.81	98.71	98.71
O	0.19	1.29	1.29
H	0.55	1.29	1.29

[a] Only species with a precent concentration greater than 1×10^{-2}% are shown.

Table 4 Percent concentrations of the species in Table 5 resulting from the kinetic model in eqn (5) as a function of time scale for the flat binding mode

	Time scale		
Species[a]	1 ns	1 μs	1 s
T = 25 °C			
CF_3CFCF_2COOH	0.52	0.52	0.52
$CF_3CF_2CF_2CO$	0.00	0.00	68.31
$CF_3CF_2CF_2COO$	99.47	99.47	31.31
CF_3CF_2CFCOO	0.00	0.00	0.09
CF_3CFCF_2COO	0.00	0.00	0.06
F	0.52	0.52	0.67
O	0.00	0.01	68.31
H	99.47	99.47	99.47
T = 100 °C			
CF_3CFCF_2COOH	1.90	1.90	1.90
$CF_3CF_2CF_2COH$	0.04	0.04	0.03
$CF_3CF_2CF_2CO$	0.00	0.05	99.42
$CF_3CF_2CF_2COO$	98.06	98.01	0.00
CF_3CF_2CFCOO	0.00	0.00	0.81
CF_3CFCF_2COO	0.00	0.00	0.54
F	1.90	1.90	3.25
O	0.04	0.09	99.45
H	98.06	98.06	98.07

[a] Only species with a precent concentration greater than 1×10^{-2}% are shown.

indicates that the reaction starts with either deprotonation or dehydroxylation reaction. At 1 μs we find the PFBA has been completely converted to $CF_3CF_2CF_2CO$ with no appreciable change in concentrations occurring between 1 μs and 1 s. While [$CF_3CF_2CF_2CO$] is 100%, we note that the concentration of surface bound OH is only 99.49% with the missing 0.51% being due to the formation of surface bound oxygen and hydrogen. These results indicate that while the dominate initial reaction of PFBA in the carbo binding mode is **R6**, we do observe **R1** and **R10** also occur (albeit as a minor side reaction) and that further degradation of PFBA would occur through a $CF_3CF_2CF_2CO$ surface species. At T = 100° the distribution of products changes; however the overall reaction pathway remains the same. Essentially we see more conversion of PFBA to $CF_3CF_2CF_2CO$ through **R6**, with some (∼1.3%) of it coming from deprotonation in **R1** followed by the deoyxgenation **R10**.

If we go through the flat binding mode PFBA (see Table 4) is fully consumed at 1 ns at T = 25°; the majority of the reaction starts with deprotonation (**R1**). However, this only accounts for 99.47% of the initial PFBA concentration. We find that by 1 ns PFBA has been partially converted into CF_3CFCF_2COOH as the C_β–F scission of **R3** occurs. Between 1 μs and 1 s we also observed a decreased concentration of $CF_3CF_2CF_2COO$ as the deprotonated PFBA product is converted into $CF_3CF_2CF_2CO$, CF_3CFCF_2COO, and CF_3CF_2CFCOO (it should be noted however the majority of the conversion results in the formation of $CF_3CF_2CF_2CO$). Increasing the temperature to 100° results in ∼4× increase in [CF_3CFCF_2OOH]; moreover, we also observe a greater concentration of the CF_3CFCF_2COO and CF_3CF_2CFCOO species from **R7** and **R8**. Curiously, at 100° we also start to observe small formations of $CF_3CF_2CF_2COH$ that result from the decarbonylation reaction in **R5**.

In summary the simplified kinetic model of eqn (5) shows us that while the carbo binding mode is more favored, PFBA is most likely to undergo dehydroxylation followed by decarbonylation (*i.e.*, **R6** → **R10**). It should also be mentioned that small amounts of products from deprotonation with a subequent decarbonylation was also detected; however the precent concentration was nearly half a percent. The flat binding mode changes this pattern; whereas no surface bound fluorine was predicted with the carbo binding mode, nearly 3% of PFBA was able to be converted to a defluorinated product. Overall our results indicate that a Fe(110) surface is capable of directly cleaving a C–F bond in PFBA as an initial reaction step.

2.4 Connection with prior experiments

While a direct comparison between the results presented above and those reported in the experimental literature is not possible owing to the complexity of the experimental systems used, we can summarize some key conclusions from the literature and from there extrapolate how our results can provide insights into these studies. We first consider the formation of F^- (or in our case, the formation of surface bound fluorine).

Liu *et al.*[125] reported using a combination of ZVI and biochar the presence of F^- with their analysis showing for PFOA ∼10% undergoes defluorination. Yan *et al.*[109] reported that ZVI under acidic conditions (pH = 3) ∼1.5% of PFOA was defluorinated. Addition of layered double hydroxide materials and persulfate increased the defluorination process by ∼0.5%. de Souza[96] also reported relatively low formation of defluorination products (0.1–2%) starting from PFOA. de Souza *et al.*[96] also reported the presence of short-chain PFAS molecules formed from the cleavage of the C–C bonds in PFOA; they hypothesize that the reaction proceeds through decarboyxlation, –CF_2– removal, then re-addition of the carboxyl group. Yang *et al.*[129] also reported defluorination; however in their study they also

treated the reaction slurry with a high concentration of NaOH. Variation of the NaOH concentration did result in lower defluorination products, indicating that the complete defluorination of PFOA reported in their paper is largely due to the presence of NaOH rather than ZVI. These experiments are (mostly) in agreement with ours: while Fe(110) can degrade the C–F bond, it does so slowly and with a low percentage of the overall PFAS. Moreover, Yan *et al.*,[109] de Souza *et al.*,[96] and Baldwin[128] all conclude that F^- removal is not the first step in the reaction pathway, in agreement with our observations. In contrast, Liu *et al.*[125] hypothesizes that ZVI can directly cleave the C–F bond, which contradicts our results as well as those discussed above.

While not featuring an iron surface, we wish to draw the attention of the reader to studies by Yuan *et al.*[158] and Wong and coworkers[159,160] due to the similarity in with our results. Yuan *et al.*[158] is a combined experimental/computational paper regarding PFOA degradation on In_2O_3 in the presence of a reducing agent. They demonstrate that PFOA binds to the In_2O_3 surface in a similar fashion to one we report here, *i.e.* through the carboxylic acid group. They also note that PFOA undergoes deprotonation followed by CO_2 removal arising from C–C_α cleavage. While we found this reaction to be unfavorable on the Fe(110) surface (see **R9** in Table 2), it is interesting that both our study and theirs demonstrate that C–F cleavage is not the first reaction step. In Biswas and Wong[159] used *ab initio* molecular dynamics with DFT to look at PFOA on γ-Al_2O_3 surfaces and observed that for γ-Al_2O_3(110) that the dominant pathway was through a C_α–C cleavage. In Sharkas and Wong[160] the Cu(111) surface in conjunction with a constant-electrode potential was used to break the C–F bonds in PFOA. With a potential of −3 V they show that C_α position gains a more negative charge, which in turn facilitates the removal of F from the carbon backbone with no degradation of the head-group.

Next, we wish to address the results of Yang *et al.*,[129] Yan *et al.*,[109] de Souza *et al.*,[96] and Baldwin,[128] who all reported the formation of iron oxides (*e.g.* magnetite, hematite, FeOOH) on the surface of the ZVI catalyst. These studies suggested that oxide formation is a byproduct of the reaction conditions; however, we would like to posit that it is possible that the iron oxides result from degradation of the –COOH head-group on the iron surface. In Tables 3 and 4 our kinetic model demonstrates that PFBA can undergo C–O scission. For the carbo binding mode this was achieved through the cleavage of the C–OH bond; for the flat binding mode it was through a C–O bond following deprotonation. We conjecture that it is the resulting surface bond oxygen species that contribute to the formation of iron oxides coupled with iron reacting with aqueous phase species. It should be noted that while the experiments cited here do not report the formation of a deoxygenated product, neither do they provide a full analysis of the decomposition products outside of whether or not it is a PFAS or a F^-.

During the review process of the current manuscript, it was brought to our attention that X-ray adsorption spectra (XAS) could be used as an analytical device for PFAS (see the work of Vo *et al.*[161] and Roesch *et al.*[162]). As this is an emerging area of research for PFAS, we utilized the GPAW implementation of Nilsson and Pettersson XAS simulation method.[163] Using a ΔKS approach we determined the core excitation of PFAS along the fluorine K-edge to be 687.50 eV, in agreement with the results from the literature.[161,162] The resulting XAS spectra for our reactions (including the initial, transition, and final states) can be found in Fig. S17—S34, in addition the vibrational density-of-states used in our thermochemical calculations are also included (see Fig. S1—S16). While a full analysis of this data is beyond the scope of the current work, it is our hope that this computational data can be used in future studies.

3 Conclusions

PFBA is a particularly harmful chemical belonging to the PFAS family of fluorocarbons. Its presence has been linked to a variety of adverse health conditions, including but not limited to, cancer and birth defects. There is a clear and present need for the design of catalytic systems that can safely and efficiently degrade PFBA and other PFAS molecules. Based on an earlier study from our group, we have identified iron as an ideal candidate for further study (and in fact, there have been several experimental papers demonstrating irons efficacy). In the current study, we expanded on our prior work by considering not only the reaction kinetics (whereas prior we were only concerned with the thermodynamics) but also included in our study several reactions besides C–F scission. In addition to the adsorption of PFBA on the Fe(110) surface, we considered a set of 10 reactions that would be primary reactions for both molecular PFBA and a its deprotonated variant. These reactions include fluorine abstraction from both the α- and β-carbon positions, as well as degradation and scission of the carboxylic acid head group.

Calculation of the requisite activation barriers and energies were then used to build a preliminary kinetic model whose primary purpose is to determine which reaction would be dominant in the initial steps of PFBA degradation on a Fe(110) surface. Our starting structures were the two binding modes (carbo and flat) that we had located in a prior study.[112] While the binding energies for both modes were within 0.1 eV of each other, the thermodynamic binding site model[148–150] shows that the carbo mode is preferred 99.6% over the flat mode. In running the kinetic model we observed that the carbo mode had no C–F scission occurring as the first step; rather the reaction would proceed through dehydroxylation/decarbonylation reactions. These reactions were also observed to be the dominant reactions for the flat mode; however we predict that 3% of the products would come from a defluorinated intermediate.

The presence of F^- in reaction media in the presence of ZVI has been reported previously. In line with our results PFAS undergoes C–F scission not as a primary reaction, but rather as a secondary reaction with a low concentration. Moreover experimental studies also indicate the presence of iron oxides; while attributed to the presence of reactive species in the reaction media, we hypothesize that iron oxide formation can occur as a result of dehydroxylation/deoxygenation of PFAS as well.

4 Computational methods

4.1 Density functional theory

The computational setup in the current study is similar to that used previously by Jenness and Shukla,[112] with a small modification. In short, GPAW[164] and the atomic simulation environment (ASE)[165] were used to performed periodic density functional theory (DFT) calculations. A three step optimization procedure with different basis sets was adopted:

1. Initial optimization performed with a linear-combination of atomic orbital (LCAO) double-ζ basis set[166]

2. Intermediate optimization with a finite-difference basis set[167,168] (grid spacing of 0.2 Å, corresponding to a kinetic energy cutoff of $\sim$900 eV[167]) at the Γ-point

3. Final optimization with finite-difference and a $(3 \times 3 \times 1)$ Monkhorst–Pack k-point mesh.[169]

All optimization steps were performed until the atomic forces were converged to 0.05 eV Å^{-1}. Periodicity was enforced in the x- and y-directions, with nonperiodicity in the z. The limited-memory Broyden–Fletcher–Goldfarb–Shanno (LBFGS)[170] and fast inertial relaxation engine (FIRE)[171] optimization methods were used as implemented in ASE. The core electrons were treated with the projector augmented wavefunction (PAW) method.[168,172,173] In all calculations, the Perdew–Burke–Ernzerhof (PBE) exchange–correlation functional[174] was utilized. The SCF procedure was converged to an energy tolerance of 1×10^{-6} eV. This is in contrast with our earlier study where we used the optPBE-vdW functional;[175,176] the reason for the switch is that we found PBE to represent the lattice parameters of iron better than the optPBE-vdW whereas in our prior study we found optPBE-vdW represented the lattice parameters of a large swath of metals better.[112] However as we are only looking at the one type of metal in this study we opted for PBE. The Fe(110) surface considered here is shown in Fig. 13 with the bcc-hollow site defined. For further details on the binding of PFBA to the Fe(110) surface we refer the reader to our previous paper,[112] and for further details on the Fe(110) surface we refer the reader to the excellent study of Błoński *et al.*[177]

Transition states were calculated using a double-constrained minimization procedure.[107] In the first step we select our reaction coordinate, typically a bond that is being broken. Initial and final states are constructed in the typical fashion.

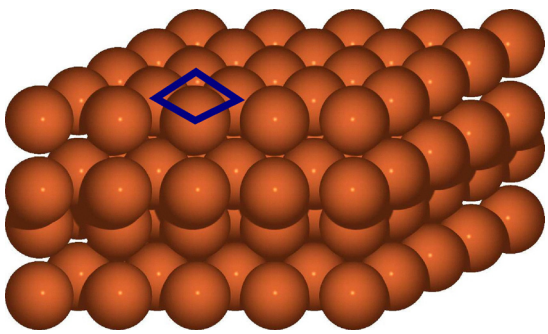

Fig. 13 Pictorial representation of the Fe(110) surface. A bcc-hollow site is defined by the blue diamond wherein the vertices are four Fe atoms.

Table 5 Reactive species from the reactions in Table 1 used in the creation of the kinetic model shown in eqn (5). All species are assumed to be surface bound

$CF_3CF_2CF_2COOH$	$CF_3CF_2CF_2COO$	OH
$CF_3CF_2CFCOOH$	CF_3CF_2CFCOO	F
CF_3CFCF_2COOH	CF_3CFCF_2COO	O
$CF_3CF_2CF_2$	$CF_3CF_2CF_2CO$	CO_2
$CF_3CF_2CF_2COH$	H	COOH

Once these two states are found, a linear interpolation between the initial and final state is done with the reaction coordinate treated as a fixed bond constraint. Each image is then minimized using the methodology laid out in the previous paragraph. When all 8 images have been minimized to a force convergence threshold of 0.05 eV Å^{-1}, the highest point is located and images on either side of it are then used as a new initial and final state. Another constrained minimization occurs and the highest energy image was selected to be the transition state. This method allows us to calculate the activation barriers efficiently and takes advantage of high-throughput computing systems. Using Hess' Law we can write the reaction energies (ΔE_{rxn}) as

$$\Delta E_{rxn} = E^{DFT}_{final\ state} - E^{DFT}_{initial\ state}, \quad (3)$$

where E^{DFT} denotes the electronic energy from our DFT calculations. With this sign convention, an exothermic reaction is one with a negative ΔE_{rxn}. The activation energy is defined as

$$E_a = E^{DFT}_{transition\ state} - E^{DFT}_{initial\ state}. \quad (4)$$

4.2 Reaction modeling

In Table 1 we list a set of ten reactions that our model is based on. Based on this set of reactions a total of fifteen intermediates can be identified (as shown in Table 5). This gives rise to the following set of coupled differential equations to be solved for,

$$\begin{aligned}\frac{d[CF_3CF_2CF_2COOH]}{dt} = {} & k_{-1}[CF_3CF_2CF_2COO][H] \\ & - k_1[CF_3CF_2CF_2COOH] \\ & + k_{-2}[CF_3CF_2CFCOOH][F] \\ & - k_2[CF_3CF_2CF_2COOH] \\ & + k_{-3}[CF_3CFCF_2COOH][F] \\ & - k_3[CF_3CF_2CF_2COOH] \\ & + k_{-4}[CF_3CF_2CF_2][COOH] \\ & - k_4[CF_3CF_2CF_2COOH] \\ & + k_{-5}[CF_3CF_2CF_2COH][O] \\ & - k_5[CF_3CF_2CF_2COOH] \\ & + k_{-6}[CF_3CF_2CF_2OH][O] \\ & - k_6[CF_3CF_2CF_2COOH] \end{aligned} \quad (5a)$$

$$\frac{d[CF_3CF_2CFCOOH]}{dt} = k_2[CF_3CF_2CF_2COOH] - k_{-2}[CF_3CF_2CFCOOH][F] \quad (5b)$$

$$\frac{d[CF_3CFCF_2COOH]}{dt} = k_3[CF_3CF_2CF_2COOH] - k_{-3}[CF_3CFCF_2COOH][F] \quad (5c)$$

$$\frac{d[CF_3CF_2CF_2]}{dt} = k_4[CF_3CF_2CF_2COOH] - k_{-4}[CF_3CF_2CF_2][COOH] + k_9[CF_3CF_2CF_2COO] - k_{-9}[CF_3CF_2CF_2][COO] \quad (5d)$$

$$\frac{d[CF_3CF_2CF_2COH]}{dt} = k_5[CF_3CF_2CF_2COOH] - k_{-5}[CF_3CF_2CF_2COH][O] \quad (5e)$$

$$\frac{d[CF_3CF_2CF_2CO]}{dt} = k_6[CF_3CF_2CF_2COOH] - k_{-6}[CF_3CF_2CF_2CO][OH] + k_{10}[CF_3CF_2CF_2COO] - k_{-10}[CF_3CF_2CF_2CO][O] \quad (5f)$$

$$\frac{d[CF_3CF_2CF_2COO]}{dt} = k_1[CF_3CF_2CF_2COOH] - k_{-1}[CF_3CF_2CF_2COO][H] + k_7[CF_3CF_2CFCOO][F] - k_{-7}[CF_3CF_2CF_2COO] + k_8[CF_3CFCF_2COO][F] - k_{-8}[CF_3CF_2CF_2COO] + k_{-9}[CF_3CF_2CF_2][CO_2] - k_9[CF_3CF_2CF_2COO] + k_{-10}[CF_3CF_2CF_2CO][O] - k_{10}[CF_3CF_2CF_2COO] \quad (5g)$$

$$\frac{d[CF_3CF_2CFCOO]}{dt} = k_7[CF_3CF_2CF_2COO] - k_{-7}[CF_3CF_2CFCOO][F] \quad (5h)$$

$$\frac{d[CF_3CFCF_2COO]}{dt} = k_8[CF_3CF_2CF_2COO] - k_{-8}[CF_3CFCF_2COO][F] \quad (5i)$$

$$\frac{d[COOH]}{dt} = k_4[CF_3CF_2CF_2COOH] - k_{-4}[CF_3CF_2CF_2][COOH] \quad (5j)$$

$$\frac{d[CO_2]}{dt} = k_9[CF_3CF_2CF_2COO] - k_{-9}[CF_3CF_2CF_2][CO_2] \quad (5k)$$

$$\frac{d[OH]}{dt} = k_6[CF_3CF_2CF_2COOH] - k_{-6}[CF_3CF_2CF_2CO][OH] \quad (5l)$$

$$\frac{d[F]}{dt} = k_2[CF_3CF_2CF_2COOH] - k_{-2}[CF_3CF_2CFCOOH][F] + k_3[CF_3CF_2CF_2COOH] - k_{-3}[CF_3CFCF_2COOH][F] + k_7[CF_3CF_2CF_2COO] - k_{-7}[CF_3CF_2CFCOO][F] + k_8[CF_3CF_2CF_2COO] - k_{-8}[CF_3CFCF_2COO][F] \quad (5m)$$

$$\frac{d[O]}{dt} = k_5[CF_3CF_2CF_2COOH] - k_{-5}[CF_3CF_2CF_2COH][O] + k_{10}[CF_3CF_2CF_2COO] - k_{-10}[CF_3CF_2CF_2CO][O] \quad (5n)$$

$$\frac{d[H]}{dt} = k_1[CF_3CF_2CF_2COOH] - k_{-1}[CF_3CF_2CF_2COO][H]. \quad (5o)$$

where k_x denotes a forward rate constant and k_{-x} denotes a reverse rate constant. Solving for the concentrations of the intermediates in Table 5 was done using the odeint module found in scipy.integrate module of the SciPy python library.[178] In eqn (5) we make two key approximations: in the first, we assume there is no desorption events. This is done so as to simplify and bring a greater degree of numerical stability to the model. In our second approximation, we assume that reactive iron sites are in excess and as a consequence we do not consider the availability of iron sites in the model. We made this approximation as PFBA has a low solubility of 304 ± 69 g L^{-1} (ref. 151) and given that experiments involving Fe^0 typically involve iron concentrations in excess of those found for PFAS molecules.[125] For the calculation of the rate constants k we employed the Eyring–Evans–Polanyi equation,[179,180]

$$k = \frac{\kappa k_B T}{h} e^{-\frac{\Delta G^{\ddagger}}{k_B T}}, \quad (6)$$

where κ is a transmission coefficient (taken here to be unity) and $\Delta G^{\ddagger}$ is the Gibbs free energy of activation. All other variables in eqn (6) have their usual thermodynamic and quantum meanings. We define $\Delta G^{\ddagger}$ as

$$\Delta G^{\ddagger} = G^{\mathrm{TS}} - G^{\mathrm{IS}}, \quad (7)$$

where G denotes the Gibbs free energy calculated in the harmonic approximation of either the transition state (TS) or initial state (IS). For the calculation of the reverse rate constant, we replace the initial state Gibbs energy with the final state Gibbs energy in eqn (7). Calculation of the vibrational frequencies required to calculate the Gibbs energy terms in eqn (7) (in addition to eqn (1)) was done through numerical differentiation of the atomic forces through the Infrared class in ASE; these frequencies where then used in the HarmonicThermo class in ASE to calculate the Gibbs free energy. In order to ensure accurate forces for the construction of the numerical Hessian, we converged the energy in the SCF procedure to 1×10^{-8} eV instead of 1×10^{-6} eV as described in Section 4.1.

Author contributions

Dr Glen R. Jenness: conceptualization, methodology, software, investigation, formal analysis, writing – original draft, writing-review & editing; Dr Manoj K. Shukla: conceptualization, methodology, writing – review & editing, supervision, projection administration, funding acquisition.

Conflicts of interest

The authors declare that they have no known competing financial interests or personal relationships that could have appeared to influence the work reported in this paper.

Data availability

The data supporting this article have been included as part of the supplementary information (SI). Supplementary information: ASE/GPAW output files in a zip archive. Bader charges, vibrational spectra, and XAS spectra are available as a PDF. See DOI: https://doi.org/10.1039/d5cp02901e.

Acknowledgements

G. R. J. would like to acknowledge Drs. Ashyln M. Koval, Timothy C. Schutt, and William A. Pisani for their feedback and comments on the current study. The use of trade, product, or firm names in this report is for descriptive purposes only and does not imply endorsement by the U.S. Government. The tests described and the resulting data presented herein, unless otherwise noted, were obtained from research conducted under the Installation and Operational Environments (IOE) RDA of USACE-ERDC. Permission was granted by the Chief of Engineers to publish this information. The findings of this report are not to be construed as an official Department of the Army position unless so designated by other authorized documents. This work was supported by a grant of computer time from the DOD High Performance Computing Modernization Program at ERDC, Vicksburg. This document has been approved for public release (Distribution Statement A).

Notes and references

1 Z. Wang, J. C. Dewitt, C. P. Higgins and I. T. Cousins, A Never-Ending Story of Per-and Polyfluoroalkyl Substances (PFASs)?, *Environ. Sci. Technol.*, 2017, **51**, 2508–2518.
2 X. C. Hu, D. Q. Andrews, A. B. Lindstrom, T. A. Bruton, L. A. Schaider, P. Grandjean, R. Lohmann, C. C. Carignan, A. Blum, S. A. Balan, C. P. Higgins and E. M. Sunderland, Detection of Poly-and Perfluoroalkyl Substances (PFASs) in U.S. Drinking Water Linked to Industrial Sites, Military Fire Training Areas, and Wastewater Treatment Plants, *Environ. Sci. Technol. Lett.*, 2016, **3**, 344–350.
3 E. Panieri, K. Baralic, D. Djukic-Cosic, A. B. Djordjevic and L. Saso, PFAS Molecules: A Major Concern for the Human Health and the Environment, *Toxics*, 2022, **10**, 44.
4 J. Glüge, M. Scheringer, I. T. Cousins, J. C. Dewitt, G. Goldenman, D. Herzke, R. Lohmann, C. A. Ng, X. Trier and Z. Wang, An Overview of the Uses of Per-And Polyfluoroalkyl Substances (PFAS), *Environ. Sci.: Proc. Imp.*, 2020, **22**, 2345–2373.
5 C. Hogue, EPA Sets Health Advisory Levels for 6 PFAS, *Chem. Eng. News*, 2022, **100**, 13.
6 EPA, EPA Announces It Will Keep Maximum Contaminant Levels for PFOA, PFOS, 2025, https://www.epa.gov/newsreleases/epa-announces-it-will-keep-maximum-contaminant-levels-pfoa-pfos.
7 Final PFAS National Primary Drinking Water Regulation, 2025, https://www.epa.gov/sdwa/and-polyfluoroalkyl-substances-pfas.
8 K. Prevedouros, I. T. Cousins, R. C. Buck and S. H. Korzeniowski, Sources, Fate and Transport of Perfluorocarboxylates, *Environ. Sci. Technol.*, 2006, **40**, 32–44.
9 M. L. Brusseau, Assessing the Potential Contributions of Additional Retention Processes to PFAS Retardation in the Subsurface, *Sci. Total Environ.*, 2018, **613–614**, 176–185.
10 R. Darlington, E. Barth and J. McKernan, The Challenges of PFAS Remediation, *Mil. Eng.*, 2018, **110**, 58–60.
11 B. M. Sharma, G. K. Bharat, S. Tayal, T. Larssen, J. Bečanová, P. Karásková, P. G. Whitehead, M. N. Futter, D. Butterfield and L. Nizzetto, Perfluoroalkyl Substances (PFAS) in River and Ground/Drinking Water of the Ganges River Basin: Emissions and Implications for Human Exposure, *Environ. Pollut.*, 2016, **208**, 704–713.
12 S. Bergström, PhD thesis, Sveriges Lantbruksuniversitet (Swedish University of Agricultural Sciences), Uppsala, Sweden, 2014.
13 A. Möller, L. Ahrens, R. Surm, J. Westerveld, F. V. D. Wielen, R. Ebinghaus and P. D. Voogt, Distribution and Sources of Poly-Fluoroalkyl Substances (PFAS) in the River Rhine Watershed, *Environ. Pollut.*, 2010, **158**, 3243–3250.

14 F. Li, C. Zhang, Y. Qu, J. Chen, L. Chen, Y. Liu and Q. Zhou, Quantitative Characterization of Short-and Long-Chain Perfluorinated Acids in Solid Matrices in Shanghai, China, *Sci. Total Environ.*, 2010, **408**, 617–623.
15 K. Y. Kwok, E. Yamazaki, N. Yamashita, S. Taniyasu, M. B. Murphy, Y. Horii, G. Petrick, R. Kallerborn, K. Kannan, K. Murano and P. K. S. Lam, Transport of Perfluoroalkyl Substances (PFAS) From an Arctic Glacier to Downstream Locations: Implications for Sources, *Sci. Total Environ.*, 2013, **447**, 46–55.
16 H. N. P. Vo, H. H. Ngo, W. Guo, T. M. H. Nguyen, J. Li, H. Liang, L. Deng, Z. Chen and T. A. H. Nguyen, Poly-and Perfluoroalkyl Substances in Water and Wastewater: A Comprehensive Review From Sources to Remediation, *J. Water Proc. Eng.*, 2020, **36**, 101393.
17 B. Xu, S. Liu, J. L. Zhou, C. Zheng, J. Weifeng, B. Chen, T. Zhang and W. Qiu, PFAS and Their Substitutes in Groundwater: Occurrence, Transformation and Remediation, *J. Hazard. Mater.*, 2021, **412**, 125159.
18 Y. H. Aly, C. Liu, D. P. McInnis, B. A. Lyon, J. Hatton, M. McCarty, W. A. Arnold, K. D. Pennell and M. F. Simcik, In Situ Remediation Method for Enhanced Sorption of Perfluoro-Alkyl Substances Onto Ottawa Sand, *J. Environ. Eng.*, 2018, **144**, 04018086.
19 Y. H. Aly, D. P. McInnis, S. M. Lombardo, W. A. Arnold, K. D. Pennell, J. Hatton and M. F. Simcik, Enhanced Adsorption of Perfluoroalkyl Substances for *In Situ* Remediation, *Environ. Sci.: Water Res. Technol.*, 2019, **5**, 1867–1875.
20 E. R. McKenzie, R. L. Siegrist, J. E. McCray and C. P. Higgins, Effects of Chemical Oxidants on Perfluoroalkyl Acid Transport in One-Dimensional Porous Media Columns, *Environ. Sci. Technol.*, 2015, **49**, 1681–1689.
21 J. Jeon, K. Kannan, B. J. Lim, K. G. An and S. D. Kim, Effects of Salinity and Organic Matter on the Partitioning of Perfluoroalkyl Acid (PFAS) to Clay Particles, *J. Environ. Monit.*, 2011, **13**, 1803–1810.
22 M. Haukås, U. Berger, H. Hop, B. Gulliksen and G. W. Gabrielsen, Bioaccumulation of Per-and Polyfluorinated Alkyl Substances (PFAS) in Selected Species From the Barents Sea Food Web, *Environ. Pollut.*, 2007, **148**, 360–371.
23 B. C. Kelly, M. G. Ikonomou, J. D. Blair, D. Hoover, R. Grace, F. A. P. C. Gobas and B. Surridge, Perfluoroalkyl Contaminants in an Arctic Marine Food Web:Trophic Magnification and Wildlife Exposure Perfluoroalkyl Contaminants in an Arctic Marine Food Web:Trophic Magnification and Wildlife Exposure, *Environ. Sci. Technol.*, 2009, 4037–4043.
24 S. Dasgupta, A. Reddam, Z. Liu, J. Liu and D. C. Volz, High-Content Screening in Zebrafish Identifies Perfluorooctanesulfonamide as a Potent Developmental Toxicant, *Environ. Pollut.*, 2020, **256**, 113550.
25 B. González-Gaya, J. Dachs, J. L. Roscales, G. Caballero and B. Jiménez, Perfluoroalkylated Substances in the Global Tropical and Subtropical Surface Oceans, *Environ. Sci. Technol.*, 2014, **48**, 13076–13084.
26 S. K. Sagiv, S. L. Rifas-Shiman, T. F. Webster, A. M. Mora, M. H. Harris, A. M. Calafat, X. Ye, M. W. Gillman and E. Oken, Sociodemographic and Perinatal Predictors of Early Pregnancy Per-and Polyfluoroalkyl Substance (PFAS) Concentrations, *Environ. Sci. Technol.*, 2015, **49**, 11849–11858.
27 EPA, Basic Information on PFAS, 2021, https://www.epa.gov/pfas/basic-information-pfas.
28 T. Pancras, G. Schrauwen, T. Held, K. Baker, I. Ross and H. Slenders, *Environmental Fate and Effects of Poly-and Perfluoroalkyl Substances (PFAS)*, 2016.
29 M.-A. Verner, A. E. Loccisano, N.-H. Morken, M. Yoon, H. Wu, R. McDougall, M. Maisonet, M. Marcus, R. Kishi, C. Miyashita, M.-H. Chen, W.-S. Hsieh, M. E. Andersen, H. J. Clewell and M. P. Longnecker, Associations of Perfluoroalkyl Substances (PFAS) With Lower Birth Weight: An Evaluation of Potential Confounding by Glomerular Filtration Rate Using a Physiologically Based Pharmacokinetic Model (PBPK), *Environ. Health Pers.*, 2015, **123**, 1317–1324.
30 F. J. Urbano and J. M. Marinas, Hydrogenolysis of Organohalogen Compounds Over Palladium Supported Catalysts, *J. Mol. Catal. A: Chem.*, 2001, **173**, 329–345.
31 S. J. Blanksby and G. B. Ellison, Bond Dissociation Energies of Organic Molecules, *Acc. Chem. Res.*, 2003, **36**, 255–263.
32 M. J. Bentel, Y. Yu, L. Xu, Z. Li, B. M. Wong, Y. Men and J. Liu, Defluorination of Per-and Polyfluoroalkyl Substances (PFASs) With Hydrated Electrons: Structural Dependence and Implications to PFAS Remediation and Management, *Environ. Sci. Technol.*, 2019, **53**, 3718–3728.
33 O. Eisenstein, J. Milani and R. N. Perutz, Selectivity of C-H Activation and Competition Between C–H and C–F Bond Activation at Fluorocarbons, *Chem. Rev.*, 2017, **117**, 8710–8753.
34 Z. Liu, M. J. Bentel, Y. Yu, C. Ren, J. Gao, V. F. Pulikkal, M. Sun, Y. Men and J. Liu, Near-Quantitative Defluorination of Perfluorinated and Fluorotelomer Carboxylates and Sulfonates With Integrated Oxidation and Reduction, *Environ. Sci. Technol.*, 2021, **55**, 7052–7062.
35 A. A. Zavitsas, The Relation Between Bond Lengths and Dissociation Energies of Carbon-Carbon Bonds, *J. Phys. Chem. A*, 2003, **107**, 897–898.
36 I. Ross, J. McDonough, J. Miles, P. Storch, P. T. Kochunarayanan, E. Kalve, J. Hurst, S. S. Dasgupta and J. Burdick, A Review of Emerging Technologies for Remediation of PFASs, *Remediation*, 2018, **28**, 101–126.
37 J. Horst, J. McDonough, I. Ross and E. Houtz, Understanding and Managing the Potential By-Products of PFAS Destruction, *Groundwater Monitor. Rem.*, 2020, **40**, 17–27.
38 R. Mahinroosta and L. Senevirathna, A Review of the Emerging Treatment Technologies for PFAS Contaminated Soils, *J. Environ. Manage.*, 2020, **255**, 109896.
39 S. Verma, T. Lee, E. Sahle-Demessie, M. Ateia and M. N. Nadagouda, Recent Advances on PFAS Degradation via Thermal and Nonthermal Methods, *Chem. Eng. J. Adv.*, 2023, **13**, 100421.
40 J. Cui, P. Gao and Y. Deng, Destruction of Per-A Nd Polyfluoroalkyl Substances (PFAS) With Advanced Reduction Processes (Arps): A Critical Review, *Environ. Sci. Technol.*, 2020, **54**, 3752–3766.

41 D. M. Wanninayake, Comparison of Currently Available PFAS Remediation Technologies in Water: A Review, *J. Environ. Manage.*, 2021, **283**, 111977.
42 D. Lu, S. Sha, J. Luo, Z. Huang and X. Z. Jackie, Treatment Train Approaches for the Remediation of Per-and Polyfluoroalkyl Substances (PFAS): A Critical Review, *J. Hazard. Mater.*, 2020, **386**, 121963.
43 N. Bolan, B. Sarkar, Y. Yan, Q. Li, H. Wijesekara, K. Kannan, D. C. Tsang, M. Schauerte, J. Bosch, H. Noll, Y. S. Ok, K. Scheckel, J. Kumpiene, K. Gobindlal, M. Kah, J. Sperry, M. B. Kirkham, H. Wang, Y. F. Tsang, D. Hou and J. Rinklebe, Remediation of Poly-and Perfluoroalkyl Substances (PFAS) Contaminated Soils -To Mobilize or to Immobilize or to Degrade?, *J. Hazard. Mater.*, 2021, **401**, 123892.
44 S. P. Lenka, M. Kah and L. P. Padhye, A Review of the Occurrence, Transformation, and Removal of Poly-and Perfluoroalkyl Substances (PFAS) in Wastewater Treatment Plants, *Water Res.*, 2021, **199**, 117187.
45 E. M. Bell, S. D. Guise, J. R. McCutcheon, Y. Lei, M. Levin, B. Li, J. F. Rusling, D. A. Lawrence, J. M. Cavallari, C. O'Connell, B. Javidi, X. Wang and H. Ryu, Exposure, Health Effects, Sensing, and Remediation of the Emerging PFAS Contaminants -Scientific Challenges and Potential Research Directions, *Sci. Total Environ.*, 2021, **780**, 146399.
46 S. E. Hale, H. P. H. Arp, G. A. Slinde, E. J. Wade, K. Bjørseth, G. D. Breedveld, B. F. Straith, K. G. Moe, M. Jartun and Å. Høisæter, Sorbent Amendment as a Remediation Strategy to Reduce PFAS Mobility and Leaching in a Contaminated Sandy Soil From a Norwegian Firefighting Training Facility, *Chemosphere*, 2017, **171**, 9–18.
47 L. Silvani, G. Cornelissen, A. B. Smebye, Y. Zhang, G. Okkenhaug, A. R. Zimmerman, G. Thune, H. Sævarsson and S. E. Hale, Can Biochar and Designer Biochar Be Used to Remediate Per-and Polyfluorinated Alkyl Substances (PFAS) and Lead and Antimony Contaminated Soils?, *Sci. Total Environ.*, 2019, **694**, 133693.
48 B. D. Turner, S. W. Sloan and G. R. Currell, Novel Remediation of Per-and Polyfluoroalkyl Substances (PFASs) From Contaminated Groundwater Using *Cannabis Sativa L.* (Hemp) Protein Powder, *Chemosphere*, 2019, **229**, 22–31.
49 A. L. Duchesne, J. K. Brown, D. J. Patch, D. Major, K. P. Weber and J. I. Gerhard, Remediation of PFAS-Contaminated Soil and Granular Activated Carbon by Smoldering Combustion, *Environ. Sci. Technol.*, 2020, **54**, 12631–12640.
50 R. McGregor, *In Situ* Treatment of PFAS-Impacted Groundwater Using Colloidal Activated Carbon, *Remediation*, 2018, **28**, 33–41.
51 D. Saha, S. Khan and S. E. V. Bramer, Can Porous Carbons Be a Remedy for PFAS Pollution in Water? A Perspective, *J. Environ. Chem. Eng.*, 2021, **9**, 106665.
52 C. G. Bresnahan, T. C. Schutt and M. K. Shukla, Exploration of Functionalizing Graphene and the Subsequent Impact on PFAS Adsorption Capabilities via Molecular Dynamics, *Chemosphere*, 2023, **345**, 140462.
53 C. G. Bresnahan, T. C. Schutt and M. K. Shukla, A Molecular Dynamics Investigation Into Manipulating Graphene Flake Spacing for Increased Selectivity Towards Short Chain PFAS Capture, *Chemosphere*, 2025, **373**, 144135.
54 X. Jiang, W. Wang, G. Yu and S. Deng, Contribution of Nanobubbles for PFAS Adsorption on Graphene and OH-And Nh2-Functionalized Graphene: Comparing Simulations With Experimental Results, *Environ. Sci. Technol.*, 2021, **55**, 13254–13263.
55 Z. Song, J. He, S. M. T. Kouzehkanan, T.-S. Oh, Y. Olshansky, E. C. Duin, K. C. Carroll and D. Wang, Enhanced Sorption and Destruction of PFAS by Biochar-Enabled Advanced Reduction Process, *Chemosphere*, 2024, **363**, 142760.
56 S. Woodard, J. Berry and B. Newman, Ion Exchange Resin for PFAS Removal and Pilot Test Comparison to GAC, *Remediation*, 2017, **27**, 19–27.
57 A. Yang, C. Ching, M. Easler, D. E. Helbling and W. R. Dichtel, Cyclodextrin Polymers With Nitrogen-Containing Tripodal Crosslinkers for Efficient PFAS Adsorption, *ACS Mater. Lett.*, 2020, **2**, 1240–1245.
58 N. A. Lundquist, M. J. Sweetman, K. R. Scroggie, M. J. Worthington, L. J. Esdaile, S. F. Alboaiji, S. E. Plush, J. D. Hayball and J. M. Chalker, Polymer Supported Carbon for Safe and Effective Remediation of Pfoa-And Pfos-Contaminated Water, *ACS Sustainable Chem. Eng.*, 2019, **7**, 11044–11049.
59 N. Saleh, A. Khalid, Y. Tian, C. Ayres, I. Sabaraya, J. Pietari, D. Hanigan, I. Chowdhury and O. Apul, Removal Of Poly-And Per-Fluoroalkyl Substances From Aqueous Systems by Nano-Enabled Water Treatment Technologies, *Environ. Sci.: Water Res. Technol.*, 2019, **5**(2), 198–208.
60 A. Pramanik, O. P. Kolawole, K. Gates, S. Kundu, M. K. Shukla, R. D. Moser, M. Ucak-Astarlioglu, A. Al-Ostaz and P. C. Ray, 2D Fluorinated Graphene Oxide (Fgo)-Polyethyleneimine (PEI) Based 3D Porous Nanoplatform for Effective Removal of Forever Toxic Chemicals, Pharmaceutical Toxins, and Waterborne Pathogens From Environmental Water Samples, *ACS Omega*, 2023, **8**, 44942–44954.
61 A. Pramanik, O. P. Kolawole, S. Kundu, K. Gates, S. Rai, M. K. Shukla and P. C. Ray, Cooperative Molecular Interaction-Based Highly Efficient Capturing of Ultrashort-and Short-Chain Emerging Per-and Polyfluoroalkyl Substances Using Multifunctional Nanoadsorbents, *ACS Omega*, 2024, 49452.
62 J. Zhang, H. Pang, S. Gray, S. Ma, Z. Xie and L. Gao, PFAS Removal From Wastewater by In-Situ Formed Ferric Nanoparticles: Solid Phase Loading and Removal Efficiency, *J. Environ. Chem. Eng.*, 2021, **9**, 105452.
63 M. Sörengård, A. S. Lindh and L. Ahrens, Thermal Desorption as a High Removal Remediation Technique for Soils Contaminated With Per-and Polyfluoroalkyl Substances (PFASs), *PLoS One*, 2020, **15**, 1–10.
64 M. Sörengård, D. B. Kleja and L. Ahrens, Stabilization and Solidification Remediation of Soil Contaminated With Poly-and Perfluoroalkyl Substances (PFASs), *J. Hazard. Mater.*, 2019, **367**, 639–646.
65 M. Sörengård, P. Gago-Ferrero, D. B. Kleja and L. Ahrens, Laboratory-Scale and Pilot-Scale Stabilization and Solidification

(S/S) Remediation of Soil Contaminated With Per-and Polyfluoroalkyl Substances (PFASs), *J. Hazard. Mater.*, 2021, **402**, 123453.

66 L. P. Turner, B. H. Kueper, K. M. Jaansalu, D. J. Patch, N. Battye, O. El-Sharnouby, K. G. Mumford and K. P. Weber, Mechanochemical Remediation of Perfluorooctanesulfonic Acid (PFOS) and Perfluorooctanoic Acid (PFOA) Amended Sand and Aqueous Film-Forming Foam (AFFF) Impacted Soil by Planetary Ball Milling, *Sci. Total Environ.*, 2021, **765**, 142722.

67 J. A. Willemsen and I. C. Bourg, Molecular Dynamics Simulation of the Adsorption of Per-and Polyfluoroalkyl Substances (PFASs) on Smectite Clay, *J. Colloid Interface Sci.*, 2021, **585**, 337–346.

68 N. Loganathan and A. K. Wilson, Adsorption, Structure, and Dynamics of Short-and Long-Chain PFAS Molecules in Kaolinite: Molecular-Level Insights, *Environ. Sci. Technol.*, 2022, **56**, 8043.

69 C. M. Luft, T. C. Schutt and M. K. Shukla, Properties and Mechanisms for PFAS Adsorption to Aqueous Clay and Humic Soil Components, *Environ. Sci. Technol.*, 2022, **56**, 10053–10061.

70 A. Valencia, D. Ordonez, A. H. Sadmani, D. Reinhart and N. B. Chang, Comparing the Removal and Fate of Long and Short Chain Per-and Polyfluoroalkyl Substances (PFAS) During Surface Water Treatment via Specialty Adsorbents, *J. Water Proc. Eng.*, 2023, **56**, 104345.

71 R. Verduzco and M. S. Wong, Fighting PFAS With PFAS, *ACS Central Sci.*, 2020, **6**, 453–455.

72 E. Kumarasamy, I. M. Manning, L. B. Collins, O. Coronell and F. A. Leibfarth, Ionic Fluorogels for Remediation of Per-And Polyfluorinated Alkyl Substances From Water, *ACS Central Sci.*, 2020, **6**, 487–492.

73 A. M. Koval, G. R. Jenness and M. K. Shukla, Structural Investigation of the Complexation Between Vitamin B12 and Per-and Polyfluoroalkyl Substances: Insights Into Degradation Using Density Functional Theory, *Chemosphere*, 2024, **364**, 143213.

74 M. Kah, D. Oliver and R. Kookana, Sequestration and Potential Release of PFAS From Spent Engineered Sorbents, *Sci. Total Environ.*, 2021, **765**, 142770.

75 J. Yu, A. Nickerson, Y. Li, Y. Fang and T. J. Strathmann, Fate of Per-and Polyfluoroalkyl Substances (PFAS) During Hydrothermal Liquefaction of Municipal Wastewater Treatment Sludge, *Environ. Sci.: Water Res. Technol.*, 2020, **6**, 1388–1399.

76 D. J. V. Hoomissen and S. Vyas, Early Events in the Reductive Dehalogenation of Linear Perfluoroalkyl Substances, *Environ. Sci. Technol. Lett.*, 2019, **6**, 365–371.

77 J. Gao, Z. Liu, M. J. Bentel, Y. Yu, Y. Men and J. Liu, Defluorination of Omega-Hydroperfluorocarboxylates (ω-HPFCAs): Distinct Reactivities From Perfluoro and Fluorotelomeric Carboxylates, *Environ. Sci. Technol.*, 2021, **55**, 14146–14155.

78 Z. Liu, Z. Chen, J. Gao, Y. Yu, Y. Men, C. Gu and J. Liu, Accelerated Degradation of Perfluorosulfonates and Perfluorocarboxylates by Uv/Sulfite + Iodide: Reaction Mechanisms and System Efficiencies, *Environ. Sci. Technol.*, 2022, **56**, 3699–3709.

79 A. M. Michalak, J. Xia, D. Brdjanovic, A.-N. Mbiyozo, D. Sedlak, T. Pradeep, U. Lall, N. Rao and J. Gupta, The Frontiers of Water and Sanitation, *Nat. Water*, 2023, **1**, 10–18.

80 S. Yang, S. Fernando, T. M. Holsen and Y. Yang, Inhibition of Perchlorate Formation During the Electrochemical Oxidation of Perfluoroalkyl Acid in Groundwater, *Environ. Sci. Technol. Lett.*, 2019, **6**, 775–780.

81 C. E. Schaefer, C. Andaya, A. Urtiaga, E. R. McKenzie and C. P. Higgins, Electrochemical Treatment of Perfluorooctanoic Acid (PFOA) and Perfluorooctane Sulfonic Acid (PFOS) in Groundwater Impacted by Aqueous Film Forming Foams (AFFFs), *J. Hazard. Mater.*, 2015, **295**, 170–175.

82 U. Rao, Y. Su, C. M. Khor, B. Jung, S. Ma, D. M. Cwiertny, B. M. Wong and D. Jassby, Structural Dependence of Reductive Defluorination of Linear PFAS Compounds in a Uv/Electrochemical System, *Environ. Sci. Technol.*, 2020, **54**, 10668–10677.

83 J. Stonebridge, R. Baldwin, N. R. Thomson and C. Ptacek, Fluoride-Selective Electrode as a Tool to Evaluate the Degradation of PFAS in Groundwater: A Bench-Scale Investigation, *Groundwater Monitor. Rem.*, 2020, **40**, 73–80.

84 P. B. Medina, V. A. Contreras, F. Hartmann, D. Schmitt, A. Klimek, J. Elbert, M. Gallei and X. Su, Investigating the Electrochemically Driven Capture and Release of Long-Chain PFAS by Redox Metallopolymer Sorbents, *ACS Appl. Mater. Interfaces*, 2023, **15**, 22112–22122.

85 N. A. Fernandez, L. Rodriguez-Freire, M. Keswani and R. Sierra-Alvarez, Effect of Chemical Structure on the Sonochemical Degradation of Perfluoroalkyl and Polyfluoroalkyl Substances (PFASs), *Environ. Sci.: Water Res. Technol.*, 2016, **2**, 975–983.

86 H. Cao, W. Zhang, C. Wang and Y. Liang, Sonochemical Degradation of Poly-and Perfluoroalkyl Substances – A Review, *Ultrason. Sonochem.*, 2020, **69**, 105245.

87 B. B. de Souza, S. A. Hewage, J. A. Kewalramani, A. C. van Duin and J. N. Meegoda, A Reaxff-Based Molecular Dynamics Study of the Destruction of PFAS Due to Ultrasound, *Environ. Pollut.*, 2023, **333**, 122026.

88 F. Laramay and M. Crimi, A Sustainability Assessment of an *In Situ* Ultrasonic Reactor for Remediation of PFAS-Contaminated Groundwater, *Remediation*, 2020, **31**, 59–72.

89 Y.-J. Lei, Y. Tian, Z. Sobhani, R. Naidu and C. Fang, Synergistic Degradation of PFAS in Water and Soil by Dual-Frequency Ultrasonic Activated Persulfate, *Chem. Eng. J.*, 2020, **388**, 124215.

90 L. Duan, B. Wang, K. Heck, S. Guo, C. A. Clark, J. Arredondo, M. Wang, T. P. Senftle, P. Westerhoff, X. Wen, Y. Song and M. S. Wong, Efficient Photocatalytic PFOA Degradation Over Boron Nitride, *Environ. Sci. Technol. Lett.*, 2020, **7**, 613–619.

91 F. Li, Z. Wei, K. He, L. Blaney, X. Cheng, T. Xu, W. Liu and D. Zhao, A Concentrate-And-Destroy Technique for

Degradation of Perfluorooctanoic Acid in Water Using a New Adsorptive Photocatalyst, *Water Res.*, 2020, **185**, 1–14.
92 S. S. Yamijala, R. Shinde, K. Hanasaki, Z. A. Ali and B. M. Wong, Photo-Induced Degradation of PFASs: Excited-State Mechanisms From Real-Time Time-Dependent Density Functional Theory, *J. Hazard. Mater.*, 2022, **423**, 127026.
93 W. Zhang, H. Cao and Y. Liang, Degradation by Hydrothermal Liquefaction of Fluoroalkylether Compounds Accumulated in Cattails (*Typha latifolia*), *J. Environ. Chem. Eng.*, 2021, **9**, 105363.
94 A. H. da, S. Filho and G. L. C. de Souza, Examining the Degradation of Environmentally-Daunting Per-and Polyfluoroalkyl Substances From a Fundamental Chemical Perspective, *Phys. Chem. Chem. Phys.*, 2020, **22**, 17659–17667.
95 M. Zhang, Y. Y. Li, X. Tian, L. Dai, G. Wang, Z. Lei, G. Ma, Q. Zuo, M. Li, M. Zhao and J. Ren, A Review of Iron-Based Catalysts for Persulfate Activation to Remove PFAS in Water: Catalytic Effects of Various Iron Species, Influencing Factors and Reaction Pathways, *Water, Air, Soil Pollut.*, 2025, **236**, 42.
96 N. G. de Souza, A. C. Parenky, H. H. Nguyen, J. Jeon and H. Choi, Removal of Perfluoroalkyl and Polyfluoroalkyl Substances in Water and Water/Soil Slurry Using Fe^0-Modified Reactive Activated Carbon Conjugated With Persulfate, *Water Environ. Res.*, 2022, **94**, e1671.
97 R. K. Singh, S. Fernando, S. F. Baygi, N. Multari, S. M. Thagard and T. M. Holsen, Breakdown Products From Perfluorinated Alkyl Substances (PFAS) Degradation in a Plasma-Based Water Treatment Process, *Environ. Sci. Technol.*, 2019, **53**, 2731–2738.
98 A. J. Lewis, T. Joyce, M. Hadaya, F. Ebrahimi, I. Dragiev, N. Giardetti, J. Yang, G. Fridman, A. Rabinovich, A. A. Fridman, E. R. McKenzie and C. M. Sales, Rapid Degradation of PFAS in Aqueous Solutions by Reverse Vortex Flow Gliding Arc Plasma, *Environ. Sci.: Water Res. Technol.*, 2020, **6**, 1044–1057.
99 D. Palma, D. Papagiannaki, M. Lai, R. Binetti, M. Sleiman, M. Minella and C. Richard, PFAS Degradation in Ultrapure and Groundwater Using Non-Thermal Plasma, *Molecules*, 2021, **26**, 1–13.
100 J. Liu and S. M. Avendano, Microbial Degradation of Polyfluoroalkyl Chemicals in the Environment: A Review, *Environ. Int.*, 2013, **61**, 98–114.
101 S. Che, B. Jin, Z. Liu, Y. Yu, J. Liu and Y. Men, Structure-Specific Aerobic Defluorination of Short-Chain Fluorinated Carboxylic Acids by Activated Sludge Communities, *Environ. Sci. Technol. Lett.*, 2021, **8**, 668–674.
102 B. Jin, Y. Zhu, W. Zhao, Z. Liu, S. Che, K. Chen, Y. H. Lin, J. Liu and Y. Men, Aerobic Biotransformation and Defluorination of Fluoroalkylether Substances (Ether PFAS): Substrate Specificity, Pathways, and Applications, *Environ. Sci. Technol. Lett.*, 2023, **10**, 755–761.
103 V. J. Scott, R. Celenligil Cetin and O. V. Ozerov, Room-Temperature Catalytic Hydrodefluorination of $C(sp^3)$–F Bonds, *J. Am. Chem. Soc.*, 2005, **127**, 2852–2853.
104 C. Douvris and O. V. Ozerov, Hydrodefluorination of Perfluoroalkyl Groups Using Silylium–Carborane Catalysts, *Science*, 2008, **321**, 1188–1190.
105 C. Douvris, C. M. Nagaraja, C. H. Chen, B. M. Foxman and O. V. Ozerov, Hydrodefluorination and Other Hydrodehalogenation of Aliphatic Carbon–Halogen Bonds Using Silylium Catalysis, *J. Am. Chem. Soc.*, 2010, **132**, 4946–4953.
106 J. Liu, D. J. V. Hoomissen, T. Liu, A. Maizel, X. Huo, S. R. Fernández, C. Ren, X. Xiao, Y. Fang, C. E. Schaefer, C. P. Higgins, S. Vyas and T. J. Strathmann, Reductive Defluorination of Branched Per-and Polyfluoroalkyl Substances With Cobalt Complex Catalysts, *Environ. Sci. Technol. Lett.*, 2018, **5**, 289–294.
107 G. R. Jenness, A. M. Koval, B. D. Etz and M. K. Shukla, Atomistic Insights Into the Hydrodefluorination of PFAS Using Silylium Catalysts, *Environ. Sci.:Processes Impacts*, 2022, **24**, 2085–2099.
108 B. Trang, Y. Li, X.-S. Xue, M. Ateia, K. N. Houk and W. R. Dichtel, Low-Temperature Mineralization of Perfluorocarboxylic Acids, *Science*, 2022, **377**, 839.
109 H. Yan, Q. Chen, Y. Lin, Y. Zu, J. Zhang, T. Feng, S. He and X. Liao, New Insights Into Removal Efficacy of Perfluoroalkyl Substances by Layered Double Hydroxide and Its Composite Materials, *Chem. Eng. J. Adv.*, 2024, **19**, 100636.
110 M. J. Krause, E. Thoma, E. Sahle-Damesessie, B. Crone, A. Whitehill, E. Shields and B. Gullett, Supercritical Water Oxidation as an Innovative Technology for PFAS Destruction, *J. Env. Eng.*, 2021, **148**, 05021006.
111 C. Austin, J. Li, S. Moore, A. Purohit, B. R. Pinkard and I. V. Novosselov, Destruction and Defluorination of PFAS Matrix in Continuous-Flow Supercritical Water Oxidation Reactor: Effect of Operating Temperature, *Chemosphere*, 2023, **327**, 138358.
112 G. R. Jenness and M. K. Shukla, What Can Blyholder Teach Us About PFAS Degradation on Metal Surfaces?, *Environ. Sci.: Adv.*, 2024, **3**, 383–401.
113 J. D. Citron, J. E. Lyons and L. H. Sommer, Palladium-Catalyzed Reactions of Triorganosilicon Hydrides With Halocarbons, *J. Org. Chem.*, 1968, **34**, 638.
114 M. Hudlicky, Catalytic Hydrogenolysis of Carbon-Fluorine Bonds: π Bond Participation Mechanism, *J. Fluorine Chem.*, 1989, **44**, 345–359.
115 A. S. Nair and T. Pradeep, Halocarbon Mineralization and Catalytic Destruction by Metal Nanoparticles, *Curr. Sci.*, 2003, **84**, 1560.
116 K. J. Stanger and R. J. Angelici, Hydrodefluorination of Fluorobenzene Catalyzed by Rhodium Metal Prepared From $[Rh(COD)_2]^+BF_4^-$ and Supported on SiO_2 and Pd–SiO_2, *J. Mol. Catal. A: Chem.*, 2004, **207**, 59–68.
117 H. R. Clark and M. M. Jones, Metal Ion Promoted Hydrolysis of Fluorocarbons, *J. Am. Chem. Soc.*, 1969, **91**, 4302.
118 E. Adisson, A. Deffieux, M. Fontanille and K. Bujadoux, Polymerization of Ethylene at High Temperature by Vanadium-Based Heterogeneous Ziegler–Natta Catalysts. II. Study of the Activation by Halocarbons, *J. Polym. Sci., Part A: Polym. Chem.*, 1994, **32**, 1033–1041.
119 J. L. Kiplinger and T. G. Richmond, Group IV Metallocene-Mediated Synthesis of Fluoroaromatics via Selective

Defluorination of Saturated Perfluorocarbons, *J. Am. Chem. Soc.*, 1996, **118**, 1805.
120 M. F. Kuehnel, D. Lentz and T. Braun, Synthesis of Fluorinated Building Blocks by Transition-Metal-Mediated Hydrodefluorination Reactions, *Angew. Chem.*, 2013, **52**, 3328–3348.
121 R. Gupta and R. D. Young, A Review on the Halodefluorination of Aliphatic Fluorides, *Synthesis*, 2022, 1671–1683.
122 M. S. Mohamed, B. P. Chaplin and A. A. Abokifa, Screening of Transition Metals for PFAS Adsorption: A Comparative DFT Investigation, *Chem. Eng. Sci.*, 2025, **307**, 121363.
123 H. Campos-Pereira, D. B. Kleja, C. Sjöstedt, L. Ahrens, W. Klysubun and J. P. Gustafsson, The Adsorption of Per- And Polyfluoroalkyl Substances (PFASs) Onto Ferrihydrite Is Governed by Surface Charge, *Environ. Sci. Technol.*, 2020, **54**, 15722–15730.
124 H. Hori, Y. Nagaoka, A. Yamamoto, T. Sano, N. Yamashita, S. Taniyasu, S. Kutsuna, I. Osaka and R. Arakawa, Efficient Decomposition of Environmentally Persistent Perfluorooctanesulfonate and Related Fluorochemicals Using Zerovalent Iron in Subcritical Water, *Environ. Sci. Technol.*, 2006, **40**, 1049–1054.
125 Y. Y. Liu, C. J. Ptacek, R. J. Baldwin, J. M. Cooper and D. W. Blowes, Application of Zero-Valent Iron Coupled With Biochar for Removal of Perfluoroalkyl Carboxylic and Sulfonic Acids From Water Under Ambient Environmental Conditions, *Sci. Total Environ.*, 2020, **719**, 137372.
126 M. S. Mohamed, B. P. Chaplin and A. A. Abokifa, Ab Initio Investigation of Per-and Poly-Fluoroalkyl Substance (PFAS) Adsorption on Zerovalent Iron (Fe^0), *ACS Omega*, 2024, 44532.
127 M. Ji, C. Christodoulatos, Q. Shi, B. Zhao, B. Smolinski, S. Sheets, G. Korfiatis and X. Meng, Kinetic and Mechanism Study of PFOS Removal by Microscale Zero-Valent Iron From Water, *Environ. Sci. Technol.*, 2025, **59**, 6297–6306.
128 J. R. Baldwin, PhD thesis, University of Waterloo, Ontario, Canada, 2018.
129 M. Yang, Z. Du, H. Bao, X. Zhang, Q. Liu, W. Guo, H. H. Ngo and L. D. Nghiem, Experimental and Theoretical Insight of Perfluorooctanoic Acid Destruction by Alkaline Hydrothermal Treatment Enhanced With Zero-Valent Iron in Biochar, *ACS EST Water*, 2023, **3**, 1286–1293.
130 L. Zhou, Z. Li, Y. Yi, E. P. Tsang and Z. Fang, Increasing the Electron Selectivity of Nanoscale Zero-Valent Iron in Environmental Remediation: A Review, *J. Hazard. Mater.*, 2022, **421**, 126709.
131 Y. Zou, X. Wang, A. Khan, P. Wang, Y. Liu, A. Alsaedi, T. Hayat and X. Wang, Environmental Remediation and Application of Nanoscale Zero-Valent Iron and Its Composites for the Removal of Heavy Metal Ions:A Review, *Environ. Sci. Technol.*, 2016, **50**, 7290–7304.
132 W. Liang, G. Wang, C. Peng, J. Tan, J. Wan, P. Sun, Q. Li, X. Ji, Q. Zhang, Y. Wu and W. Zhang, Recent Advances of Carbon-Based Nano Zero Valent Iron for Heavy Metals Remediation in Soil and Water: A Critical Review, *J. Hazard. Mater.*, 2022, **426**, 127993.
133 J. Zhao, D. T. Lee, R. W. Yaga, M. G. Hall, H. F. Barton, I. R. Woodward, C. J. Oldham, H. J. Walls, G. W. Peterson and G. N. Parsons, Ultra-Fast Degradation of Chemical Warfare Agents Using MOF– Nanofiber Kebabs Angewandte, *Angew. Chem., Int. Ed.*, 2016, **55**, 13224–13228.
134 Q. Wu, Y. Sun, Z. Luo, X. Li, Y. Wen, Y. Shi, X. Wu, X. Huang, Y. Zhu and C. Huang, Application and Development of Zero-Valent Iron (Zvi)-Based Materials for Environmental Remediation: A Scientometric and Visualization Analysis, *Environ. Res.*, 2024, **241**, 117659.
135 F. Fu, D. D. Dionysiou and H. Liu, The Use of Zero-Valent Iron for Groundwater Remediation and Wastewater Treatment: A Review, *J. Hazard. Mater.*, 2014, **267**, 194–205.
136 Y. Liu and J. Wang, Reduction of Nitrate by Zero Valent Iron (Zvi)-Based Materials: A Review, *Sci. Total Environ.*, 2019, **671**, 388–403.
137 S. Zhang, K. Li, Y. Ma, F. Guo, C. Jiang, Z. Liang, Y. Bu and J. Zhang, Density Functional Studies on the Atomistic Structure and Properties of Iron Oxides: A Parametric Study, *Materials*, 2022, **15**, 8316.
138 O. of Toxicity Assessment'', *Health Advisory Update for Perfluorobutanoic Acid (PFBA) Chemical Abstract Services Registry Number (CASRN) 375-22-4*, Illinois environmental protection agency technical report, 2025.
139 G. A. Picayo, B. D. Etz, S. Vyas and M. P. Jensen, Characterization of the ALSEP Process at Equilibrium: Speciation and Stoichiometry of the Extracted Complex, *ACS Omega*, 2020, **5**, 8076–8089.
140 G. Blyholder and W. V. Wyatt, Infrared Spectra and Structures of Some C_xH_yO Compounds Adsorbed on Silica-Supported Iron, Cobalt, and Nickel, *J. Phys. Chem.*, 1966, **70**, 1745–1750.
141 R. Madix, J. Falconer and A. Suszko, The Autocatalytic Decomposition of Acetic Acid on Ni(110), *Surf. Sci.*, 1976, **54**, 6–20.
142 G. Blyholder, D. Shihabi, W. V. Wyatt and R. Bartlett, Adsorption and Interaction of C_2H_4, H_2, CO, and Organic Acids on Fe, Co, and Ni, *J. Catal.*, 1976, **43**, 122.
143 J. Benziger and R. J. Madix, Reactions and Reaction Intermediates on Iron Surfaces I. Methanol, Ethanol, and Isopropanol on Fe(100), *J. Catal.*, 1980, **65**, 36–48.
144 J. B. Benziger' and R. J. Madix, Reactions and Reaction Intermediates on Iron Surfaces II. Hydrocarbons and Carboxylic Acids, *J. Catal.*, 1980, **65**, 49.
145 R. J. Jouet, A. D. Warren, D. M. Rosenberg, V. J. Bellitto, K. Park and M. R. Zachariah, Surface Passivation of Bare Aluminum Nanoparticles Using Perfluoroalkyl Carboxylic Acids, *Chem. Mater.*, 2005, **17**, 2987–2996.
146 Q. Gu, P. Sautet and C. Michel, Unraveling the Role of Base and Catalyst Polarization in Alcohol Oxidation on Au and Pt in Water, *ACS Catal.*, 2018, **8**, 11716–11721.
147 M. Boronat, A. Corma, F. Illas, J. Radilla, T. Ródenas and M. J. Sabater, Mechanism of Selective Alcohol Oxidation to Aldehydes on Gold Catalysts: Influence of Surface Roughness on Reactivity, *J. Catal.*, 2011, **278**, 50–58.

148 G. R. Jenness, S. A. Giles and M. K. Shukla, Thermodynamic Adsorption States of TNT and DNAN on Corundum and Hematite, *J. Phys. Chem. C*, 2020, **124**, 13837–13844.
149 G. R. Jenness and M. K. Shukla, Effect of Concrete Composition on the Thermodynamic Binding of Dopamine: A DFT Study, *Langmuir*, 2021, **38**, 472–481.
150 W. A. Pisani, G. R. Jenness, T. C. Schutt, S. L. Larson and M. K. Shukla, Preferential Adsorption of Prominent Amino Acids in the Urease Enzyme of ⟨*I*⟩ Sporosarcina Pasteurii ⟨*I*⟩ on Arid Soil Components: A Periodic DFT Study, *Langmuir*, 2022, **38**, 13414–13428.
151 W. C. Kwan, PhD thesis, University of Toronto, 2001.
152 R. Bader, *Atoms in Molecules: A Quantum Theory*, Clarendon, 1994.
153 G. Henkelman, A. Arnaldsson and H. Jónsson, A Fast and Robust Algorithm for Bader Decomposition of Charge Density, *Comput. Mater. Sci.*, 2006, **36**, 354–360.
154 E. Sanville, S. D. Kenny, R. Smith and G. Henkelman, Improved Grid-Based Algorithm for Bader Charge Allocation, *J. Comput. Chem.*, 2007, **28**, 899–908.
155 W. Tang, E. Sanville and G. Henkelman, A Grid-Based Bader Analysis Algorithm Without Lattice Bias, *J. Phys.: Condens. Matter: Institute Phys. J.*, 2009, **21**, 084204.
156 S. Chrétien and H. Metiu, Density Functional Study of the Charge on Au_n Clusters (n = 1–7) Supported on a Partially Reduced Rutile TiO_2(110): Are All Clusters Negatively Charged?, *J. Chem. Phys.*, 2007, **126**, 104701.
157 S. Chrétien and H. Metiu, Density Functional Study of the Interaction Between Small Au Clusters, Au_n (N = 1-7) and the Rutile TiO_2 Surface II: Adsorption on a Partially Reduced Surface, *J. Chem. Phys.*, 2007, **127**, 244708.
158 Y. Yuan, L. Feng, X. He, X. Liu, N. Xie, Z. Ai, L. Zhang and J. Gong, Efficient Removal of PFOA With an In_2O_3/persulfate System Under Solar Light *via* the Combined Process of Surface Radicals and Photogenerated Holes, *J. Hazard. Mater.*, 2022, **423**, 127176.
159 S. Biswas and B. M. Wong, Degradation of Perfluorooctanoic Acid on Aluminum Oxide Surfaces: New Mechanisms From Ab Initio Molecular Dynamics Simulations, *Environ. Sci. Technol.*, 2023, **57**, 6695–6702.
160 K. Sharkas and B. M. Wong, Defluorination Mechanisms and Real-Time Dynamics of Per-and Polyfluoroalkyl Substances on Electrified Surfaces, *Environ. Sci. Technol. Lett.*, 2025, **12**, 230–236.
161 P. H. Vo, C. Vogel, H. T. Nguyen, B. R. Hamilton, P. K. Thai, P. Roesch, F. G. Simon and J. F. Mueller, μ-X-ray Fluorescence (XRF) and Fluorine K-Edge μ-X-ray Absorption Near-Edge Structure (XANES) Spectroscopy for Detection of PFAS Distribution in the Impacted Concrete, *J. Hazard. Mater. Lett.*, 2024, **5**, 100134.
162 P. Roesch, C. Vogel, T. Huthwelker, P. Wittwer and F. G. Simon, Investigation of Per-and Polyfluoroalkyl Substances (PFAS) in Soils and Sewage Sludges by Fluorine K-Edge XANES Spectroscopy and Combustion Ion Chromatography, *Environ. Sci. Pollut. Res.*, 2022, **29**, 26889–26899.
163 A. Nilsson and L. G. M. Pettersson, Chemical Bonding on Surfaces Probed by X-Ray Emission Spectroscopy and Density Functional Theory, *Surf. Sci. Rep.*, 2004, **55**, 49–167.
164 J. Enkovaara, C. Rostgaard, J. J. Mortensen, J. Chen, M. Dułak, L. Ferrighi, J. Gavnholt, C. Glinsvad, V. Haikola, H. A. Hansen, H. H. Kristoffersen, M. Kuisma, A. H. Larsen, L. Lehtovaara, M. Ljungberg, O. Lopez-Acevedo, P. G. Moses, J. Ojanen, T. Olsen, V. Petzold, N. A. Romero, J. Stausholm-Møller, M. Strange, G. A. Tritsaris, M. Vanin, M. Walter, B. Hammer, H. Håkkinen, G. K. H. Madsen, R. M. Nieminen, J. K. Nørskov, M. Puska, T. T. Rantala, J. Schiøtz, K. S. Thygesen and K. W. Jacobsen, Electronic Structure Calculations With GPAW: A Real-Space Implementation of the Projector Augmented-Wave Method, *J. Phys.: Condens. Matter*, 2010, **22**, 253202–253226.
165 A. H. Larsen, J. J. Mortensen, J. Blomqvist, I. E. Castelli, R. Christensen, M. Dułak, J. Friis, M. N. Groves, B. Hammer, C. Hargus, E. D. Hermes, P. C. Jennings, P. B. Jensen, J. Kermode, J. R. Kitchin, E. L. Kolsbjerg, J. Kubal, K. Kaasbjerg, S. Lysgaard, J. B. Maronsson, T. Maxson, T. Olsen, L. Pastewka, A. Peterson, C. Rostgaard, J. Schiøtz, O. Schütt, M. Strange, K. S. Thygesen, T. Vegge, L. Vilhelmsen, M. Walter, Z. Zeng and K. W. Jacobsen, The Atomic Simulation Environment-A Python Library for Working With Atoms, *J. Phys.: Condens. Matter*, 2017, **29**, 273002.
166 A. H. Larsen, M. Vanin, J. J. Mortensen, K. S. Thygesen and K. W. Jacobsen, Localized Atomic Basis Set in the Projector Augmented Wave Method, *Phys. Rev. B: Condens. Matter Mater. Phys.*, 2009, **80**, 195112.
167 E. Briggs, D. Sullivan and J. Bernholc, Real-Space Multigrid-Based Approach to Large-Scale Electronic Structure Calculations, *Phys. Rev. B: Condens. Matter Mater. Phys.*, 1996, **54**, 14362–14375.
168 J. Mortensen, L. Hansen and K. Jacobsen, Real-Space Grid Implementation of the Projector Augmented Wave Method, *Phys. Rev. B: Condens. Matter Mater. Phys.*, 2005, **71**, 035109.
169 H. J. Monkhorst and J. D. Pack, Special Points for Brillouin-Zone Integrations, *Phys. Rev. B: Condens. Matter Mater. Phys.*, 1976, **13**, 5188–5192.
170 D. C. Liu and J. Nocedal, On the Limited Memory BFGS Method for Large Scale Optimization, *Math. Prog.*, 1989, **45**, 503–528.
171 E. Bitzek, P. Koskinen, F. Gåhler, M. Moseler and P. Gumbsch, Structural Relaxation Made Simple, *Phys. Rev. Lett.*, 2006, **97**, 1–4.
172 P. E. Blöchl, Projector Augmented-Wave Method, *Phys. Rev. B: Condens. Matter Mater. Phys.*, 1994, **50**, 17953–17979.
173 G. Kresse, From Ultrasoft Pseudopotentials to the Projector Augmented-Wave Method, *Phys. Rev. B: Condens. Matter Mater. Phys.*, 1999, **59**, 1758–1775.
174 J. P. Perdew, K. Burke and M. Ernzerhof, Generalized Gradient Approximation Made Simple, *Phys. Rev. Lett.*, 1996, **77**, 3865–3868.
175 J. Klimeš, D. R. Bowler and A. Michaelides, Chemical Accuracy for the van der Waals Density Functional, *J. Phys.: Condens. Matter*, 2010, **22**, 022201.

176 J. Klimeš, D. R. Bowler and A. Michaelides, van der Waals Density Functionals Applied to Solids, *Phys. Rev. B*, 2011, **83**, 1–13.
177 P. Błoński and A. Kiejna, Structural, Electronic, and Magnetic Properties of Bcc Iron Surfaces, *Surf. Sci.*, 2007, **601**, 123–133.
178 P. Virtanen, R. Gommers, T. E. Oliphant, M. Haberland, T. Reddy, D. Cournapeau, E. Burovski, P. Peterson, W. Weckesser, J. Bright, S. J. van der Walt, M. Brett, J. Wilson, K. J. Millman, N. Mayorov, A. R. Nelson, E. Jones, R. Kern, E. Larson, C. J. Carey, I. Polat, Y. Feng, E. W. Moore, J. VanderPlas, D. Laxalde, J. Perktold, R. Cimrman, I. Henriksen, E. A. Quintero, C. R. Harris, A. M. Archibald, A. H. Ribeiro, F. Pedregosa, P. van Mulbregt, A. Vijaykumar, A. P. Bardelli, A. Rothberg, A. Hilboll, A. Kloeckner, A. Scopatz, A. Lee, A. Rokem, C. N. Woods, C. Fulton, C. Masson, C. Häggström, C. Fitzgerald, D. A. Nicholson, D. R. Hagen, D. V. Pasechnik, E. Olivetti, E. Martin, E. Wieser, F. Silva, F. Lenders, F. Wilhelm, G. Young, G. A. Price, G. L. Ingold, G. E. Allen, G. R. Lee, H. Audren, I. Probst, J. P. Dietrich, J. Silterra, J. T. Webber, J. Slavič, J. Nothman, J. Buchner, J. Kulick, J. L. Schönberger, J. V. de Miranda Cardoso, J. Reimer, J. Harrington, J. L. C. Rodríguez, J. Nunez-Iglesias, J. Kuczynski, K. Tritz, M. Thoma, M. Newville, M. Kümmerer, M. Bolingbroke, M. Tartre, M. Pak, N. J. Smith, N. Nowaczyk, N. Shebanov, O. Pavlyk, P. A. Brodtkorb, P. Lee, R. T. McGibbon, R. Feldbauer, S. Lewis, S. Tygier, S. Sievert, S. Vigna, S. Peterson, S. More, T. Pudlik, T. Oshima, T. J. Pingel, T. P. Robitaille, T. Spura, T. R. Jones, T. Cera, T. Leslie, T. Zito, T. Krauss, U. Upadhyay, Y. O. Halchenko and Y. Vázquez-Baeza, Scipy 1.0: Fundamental Algorithms for Scientific Computing in Python, *Nat. Methods*, 2020, **17**, 261–272.
179 H. Eyring, The Activated Complex in Chemical Reactions, *J. Chem. Phys.*, 1935, **3**, 107–115.
180 M. G. Evans and M. Polanyi, Some Applications of the Transition State Method to the Calculation of Reaction Velocities, Especially in Solution, *Trans. Faraday Soc.*, 1935, **31**, 875.

